
COMPUTATIONAL FRAMEWORK FOR MONOLITHIC COUPLING FOR THIN FLUID FLOW IN CONTACT INTERFACES

Andrei G. Shvarts^{1,2*}, Julien Vignollet³, and Vladislav A. Yastrebov¹

¹*MINES ParisTech, PSL Research University, Centre des Matériaux, CNRS UMR 7633,
BP 87, 91003 Evry, France*

²*Glasgow Computational Engineering Centre, School of Engineering, University of Glasgow,
G12 8QQ Glasgow, United Kingdom*

³*Safran Tech, Safran Group, 1 rue Geneviève Aube, 78114 Magny-les-Hameaux, France*

Abstract

We develop a computational framework for simulating thin fluid flow in narrow interfaces between contacting solids, which is relevant for a range engineering, biological and geophysical applications. The treatment of this problem requires coupling between fluid and solid mechanics equations, further complicated by contact constraints and potentially complex geometrical features of contacting surfaces. We develop a monolithic finite-element framework for handling contact, thin incompressible viscous flow and fluid-induced tractions on the surface of the solid, suitable for both one- and two-way coupling approaches. Additionally, we consider fluid entrapment in “pools” delimited by contact patches and its pressurisation following a non-linear compressible constitutive law. Image analysis algorithms are adopted to identify the local status of each interface element (i.e. distinguish between contact, fluid flow and trapped fluid zones) within the Newton convergence loop. First, an application of the proposed framework for a problem with a model geometry is given, and the robustness is demonstrated by the DOF-wise and status-wise convergence. The full capability of the developed two-way coupling framework is demonstrated on a problem of a fluid flow in a contact interface between a solid with representative rough surface and a rigid flat. The evolution of the contact pressure, fluid flow pattern and the morphology of trapped fluid zones under increasing external load until the complete sealing of the interface is displayed. Finally, effective properties of flat-on-flat rough contact interfaces such as transmissivity and real contact area growth are calculated using the developed framework, showing qualitatively new results compared to the one-way coupling approximation.

Keywords Finite-element method · mechanical contact · thin fluid flow · trapped fluid · monolithic coupling

1 Introduction

The problem of thin fluid flow in narrow interfaces between contacting or slightly separated deformable solids appears in different contexts: in engineering and biological applications, as well as in geophysical sciences. Rigorous handling of such problems requires solution of a strongly nonlinear contact problem, which is further complicated by a multi-field coupling of essentially interrelated fluid and solid mechanics. The free volume² between contacting surfaces depends on their initial geometry, which can be rather complex: they may have deterministic features (e.g. turned (Pérez-Ràfols et al., 2016), patterned surfaces (Sahlin et al., 2010b; Prodanov et al., 2013)) and, at a certain magnification, may be considered as randomly rough (Nayak, 1971) down to atomistic scale (Krim and Palasantzas, 1995; Ponson et al., 2006; Whitehouse, 2010; Thomas, 1999).

*Corresponding author: andrei.shvarts@glasgow.ac.uk

²By free volume, here, we mean the void separating the contacting surfaces.

Numerous applications of the problem of thin fluid flow in contact interfaces include sealing engineering (Müller and Nau, 1998), lubrication in elasto-hydrodynamic and mixed regimes (Stupkiewicz and Marcinişzyn, 2009; Sahlin et al., 2010a) and functioning of human joints (Caligaris and Ateshian, 2008). Such an interaction between fluids and solids in contact is also relevant for hydraulic fracturing (Bařant et al., 2014), extraction of shale gas and oil from rocks (Hubbert and Willis, 1972), and at larger scales in landslides (Viesca and Rice, 2012), slip in pressurized faults (Garagash and Germanovich, 2012) and basal sliding of glaciers (Fischer and Clarke, 1997).

The problem under discussion belongs to a vast domain of fluid-structure interaction (FSI) problems, which involve deformation and/or motion of the solids interacting with the internal and/or external fluid(s). These problems are of very wide range, spanning from deformation of airplane wings and rotor blades subjected to the sub- or supersonic air flow (Farhat et al., 2003; Bazilevs et al., 2011) to modelling of the blood flow (Bazilevs et al., 2006; Gerbeau and Vidrascu, 2003) and heart valves (Dos Santos et al., 2008; Astorino et al., 2009; Kamensky et al., 2015), scaling up to suspended bridge instabilities under wind load (Païdoussis et al., 2010), ship stability (Wackers et al., 2011) or huge iceberg’s capsizes in water (Sergeant et al., 2018). All these problems correspond to different space and time scales, operating conditions and other requirements, therefore a unified FSI approach fit for all cases does not exist, and different techniques have been developed for particular problems.

Many problems of the fluid-structure interaction, such as aeroelasticity and hemodynamics, correspond to the case of the high-Reynolds-number flow. Therefore, different mesh density, and often different time stepping, are required for the solid and fluid domains. Furthermore, the fluid domain evolves due to motion and deformation of solids. A number of methods have been used to overcome the associated computational complexity, such as arbitrary Lagrangian-Eulerian method (Donea et al., 1982; Takashi and Hughes, 1992; Wick, 2014), fictitious domain method (Baaijens, 2001; De Hart et al., 2003; Dos Santos et al., 2008), immersed boundary method (Mittal and Iaccarino, 2005; Kadapa et al., 2017) and extended finite element method (Mayer et al., 2010; Gerstenberger and Wall, 2008). On the contrary, fluid flow in contacting or slightly separated interfaces is usually of low Reynolds number and, moreover, the thickness of the fluid film is usually much smaller than other dimensions of the solid. In this case general Navier-Stokes equations could be readily simplified down to the Reynolds equation for the viscous flow (Hamrock et al., 2004). This simplification permits to use compatible meshes for the fluid and the solid domains and, under assumption of constant pressure through the film thickness, define the Reynolds equation on the so-called lubrication surface, so that specific methods discussed above are not required, see (Stupkiewicz and Marcinişzyn, 2009; Stupkiewicz et al., 2016).

From the point of view of the underlying physical processes, different FSI strategies could be divided into one-way and two-way coupling approaches. In the context of thin fluid flow through contact interfaces, the former implies that the solution of the solid mechanics problem defines the distribution of the free volume in the interface which can be occupied by the fluid flow, however the fluid pressure does not affect the deformation of the solids, i.e. the fluid problem is solved assuming rigid walls of solids. In the two-way coupling this approximation is dropped, and the fluid-induced traction acting on the surface of the deformable solid is taken into account.

In elasto-hydrodynamic lubrication regime, as well as for non-contact seals, the two-way coupling is often used, see (Stupkiewicz and Marcinişzyn, 2009; Stupkiewicz et al., 2016; Yang and Laursen, 2009). However, for the important case of contact seals, or, more generally, if contact is present in the interface, the one-way coupling is rather utilized, see (Dapp et al., 2012; Dapp and Müser, 2016; Pérez-Ràfols et al., 2016). It is widely assumed in this context that the deformation of the solids happens mainly due to the contact interaction, and the fluid pressure effect on the solid is negligible, since the contact pressure at surface’s asperities is considerably higher than the physically relevant fluid pressure. However, to the best of authors knowledge, a quantitative range of validity of one-way coupling for problems involving thin fluid flow in contact interfaces, depending on the surface geometry, material properties and the fluid pressure, has not been determined yet. The lack of such quantitative analysis is probably caused by insufficiency of existing numerical methods for comparison of one- and two-way coupling approaches for these problems, which is the main motivation of the current study.

It is important to note, that the application of the above mentioned rather general FSI approaches to problems involving solid-solid contact provide possibility for two-way coupling, see e.g. (Mayer et al., 2010; Kamensky et al., 2015). However, these methods become inefficient if a very fine discretization is used to accurately represent surface roughness in a numerical simulation. This computational complexity can be overcome by considering surface roughness in an averaged sense at the macroscopic level, see (Patir and Cheng, 1978;

Pérez-Ràfols et al., 2016; Zaouter et al., 2018; Waseem et al., 2017), or as was done recently using a porous flow model (Ager et al., 2018). Nonetheless, if one is interested in the effect of rough or deterministic surface features on the solution of the coupled problem, e.g. distribution of contact stresses and fluid flow patterns, this approximation is not appropriate. Therefore, the main purpose of the current study is to develop a computational framework suitable for both one- and two-way coupling approaches and applicable for a discretization which reflects essential features of the surface geometry.

An important example of the effect of the surface roughness on the coupled problem, relevant only for the two-way coupling, is the phenomenon of fluid entrapment. Indeed, studying the evolution of the morphology of the contact interface under increasing normal load, one may observe how non-simply connected contact patches appear, see (Yastrebov et al., 2015; Lorenz and Persson, 2010). At the same time, the fluid present in the interface can be trapped inside “pools” or “valleys” bounded by these patches and subsequently become pressurized and provide additional load-bearing capacity. The behaviour of trapped fluid accounts for a significant reduction of friction in tire-road contact (Scaraggi and Persson, 2012), cold metal forming (Azushima and Kudo, 1995) and functioning of human joints (Soltz et al., 2003; Chan et al., 2011). However, the effect of the fluid entrapment on transmissivity of contact interfaces, which is an important characteristic for sealing engineering, has not been thoroughly investigated yet.

We have recently studied the behaviour of hydrostatically pressurized fluid trapped in a contact interface without considering the fluid flow (Shvarts and Yastrebov, 2018b). We used the augmented Lagrangian method for the contact constraints, and the classic Lagrange multiplier method permitted us to take into account the additional constraint in case of incompressible fluid, while the penalty method was applied if the fluid was assumed compressible. We introduced a novel trapped fluid super-element based on all out-of-contact segments (faces in 3D), surrounded by a contact patch, so that displacements of all nodes associated with this element were included into its degrees of freedom (DOF) vector. Moreover, we proposed a technique of extension of the trapped fluid element on the surrounding contact zone by superposing locally the contact and fluid pressure fields, which simplified considerably computations in certain cases (see Appendix B in (Shvarts and Yastrebov, 2018b)). Therefore, an additional objective of the current study is to incorporate the formulation of the trapped fluid element into the computational framework, permitting to quantify the effect of trapped fluid zones on the coupled problem.

From the implementation point of view two distinct approaches for any FSI problem exist: partitioned and monolithic. The former is based on two different solvers for the fluid and solid sub-problems, and in order to take into account the coupling, one- or two-way data exchange between them must be established. Furthermore, a certain iterative process is required to obtain the convergence. The utilization of the partitioned approach benefits from modularity, since different solvers tailored for the sub-problems could be used (Küttler and Wall, 2008; Matthies and Steindorf, 2003), however, convergence and stability of such scheme could raise issues, and special techniques may become necessary, see, for example (Heil, 1998). On the contrary, under the *monolithic* approach all equations which govern sub-problems and the interaction between them are rendered into one system, and upon its solution DOF values corresponding to both sub-problems are obtained simultaneously (Hübner et al., 2004; Michler et al., 2004; Heil, 2004; Verdugo and Wall, 2016). The data exchange in this case is not needed, the stability and convergence are obtained easier, however, solution of the vast system of algebraic equations is necessary. Nevertheless, for the problem under discussion this last issue is not relevant, since the number of unknowns in the interface is considerably smaller than in the bulk of the solid, if, for example, finite-element discretization is used.

Elasto-hydrodynamic lubrication problems are often solved under the monolithic approach (Stupkiewicz et al., 2016; Stupkiewicz and Marciniszyn, 2009; Yang and Laursen, 2009), whilst for the contact sealing problems the partitioned approach is generally preferred (Pérez-Ràfols et al., 2016). Moreover, as was already mentioned above, the problem is often solved under the one-way coupling approach, using the assumption of the infinitesimal slopes of the surface profile and the small deformation formulation. Boundary element method (Pérez-Ràfols et al., 2016) and Green’s function molecular dynamics (Dapp et al., 2012) are frequently used for the mechanical contact problem and the Reynolds equation is often solved by the finite-differences method.

In this paper we develop a computational framework aimed first at resolution of the two-way coupling of the mechanical contact and fluid flow sub-problems, which could require rather frequent and considerable data exchange in case of the partitioned approach. The second objective is to take into account the effect of trapped fluid pools appearing in the interface. If the number of these zones becomes large, then a resolution under the partitioned approach becomes even more complicated, since the history tracking of trapped zones is needed. The *monolithic* approach appears beneficial for our purposes and, therefore, it was applied throughout this

study. We use the finite-element method in order to make possible application of the proposed framework for different surface geometries (e.g. with finite slopes of the profile), under larger deformation formulation and with different material models of the solid (e.g. elasto-plastic, viscoelastic, etc). The Newton-Raphson method is applied to solve the essentially nonlinear problem, and, furthermore, on each iteration we perform identification of the local status in the interface to distinguish between contact zones and fluid flow zones and also keep track of formation and evolution of trapped fluid pools.

Note that the methodology presented here was already applied to a two-way coupling problem of a pressure driven fluid flow in contact interface between an elastic solid with an extruded wavy surface and a rigid flat (Shvarts and Yastrebov, 2018a). In the same paper we derived an approximate analytical formula based on the Westergaard-Kuznetsov solution (Westergaard, 1939; Kuznetsov, 1985) and a one-dimensional formulation of Reynolds equation, which describes both the solid deformation and the fluid pressure distribution in case of two-way coupling. The comparison of this approximation with a numerical solution based on the presented framework showed good agreement between the two in the interval of loads within which the analytical one is applicable. Furthermore, the numerical method permitted us to investigate the problem with parameters beyond the range of validity of the analytical solution up to full sealing of the interface. However, since only regular wavy profiles were studied, the problem did not include trapped fluid zones, therefore a complete testing of the proposed method was not possible. Moreover, the methodology was only used, and was not discussed in detail in the above cited work.

The present paper is organized as follows. In Section 2 we formulate the coupled problem by outlining equations governing each sub-part of it, while Section 3 introduces the variational statement for this problem under both one- and two-way coupling approaches. In Section 4 we propose the monolithic framework and provide ready-to-implement finite-element formulations of the tangent matrix and the residual vector of the coupled problem. Moreover, we discuss the algorithm used to determine the local status in the interface and keep track of formation and evolution of multiple trapped fluid zones. Section 5 is devoted to examples showing capabilities of the proposed framework and some relevant discussions. Finally, Section 6 provides a short conclusion.

2 Problem statement

We consider the problem of a thin fluid flow in contact interface between a solid body with an arbitrary surface geometry, given, for concreteness, by a function $z(x, y)$, and a rigid flat described by a plane $z = 0$. This set-up was chosen to simplify the formulation of the contact problem and to concentrate the discussion on handling of the fluid/solid coupling. Note that the unilateral contact set-up is equivalent to the case of contact between two deformable bodies under linear isotropic elasticity and infinitesimal strain assumptions, see (Barber, 2013). Furthermore, the problem statement with one of the contacting solids considered as rigid is relevant when the elasticity modulus of this solid is considerably higher than of the other, which is the case, for example, in rubber sealing applications (Persson and Yang, 2008) and in tire-road contact (Scaraggi and Persson, 2012). At the same time, the numerical framework developed in this paper for the case of unilateral contact can be extended afterwards to the problem of contact between two deformable solids with arbitrary surface geometries.

Let us denote by Ω the deformable solid and by $\Gamma \subset \partial\Omega$ the part of its surface which represents the *potential* contact zone, i.e. defines the extent of the contact interface. The resolution of the coupled problem requires subdivision of the surface Γ into following parts, according to the local status³ of the interface, see Fig. 1:

$$\Gamma = \Gamma^c \cup \Gamma^{\text{fsi}} \bigcup_{i=1}^{n_{\text{tf}}} \Gamma_i^{\text{tf}}, \quad (1)$$

where Γ^c is the *active* contact zone where normal contact tractions are non-zero, Γ^{fsi} is the part of the solid's surface which interacts with the flowing fluid and where the surface tractions are equal to the corresponding tractions in the fluid (so-called *fluid-structure interface*), Γ_i^{tf} , $i = \overline{1, n_{\text{tf}}}$ are *trapped fluid* zones, i.e. parts of the surface Γ which are out of contact, but completely delimited by non-simply connected contact patches. Furthermore, we term by Γ^{f} the projection of Γ^{fsi} on the plane $z = 0$, which serves as the lubrication surface where the Reynolds equation for the fluid flow will be defined.

By definition, $\Gamma^c \cap \Gamma^{\text{fsi}} = \emptyset$ and $\Gamma^c \cap \Gamma_i^{\text{tf}} = \emptyset \forall i = \overline{1, n_{\text{tf}}}$. Note also, that $\Gamma^{\text{fsi}} \cap \Gamma_i^{\text{tf}} = \emptyset \forall i = \overline{1, n_{\text{tf}}}$, i.e. even though all trapped pockets contain the same fluid, as the one present in the fluid-flow domain, the behaviour

³By the local status in this context we mean the location of each point of the solid's surface in the active contact zone, fluid-structure interface, or one of the trapped fluid zones.

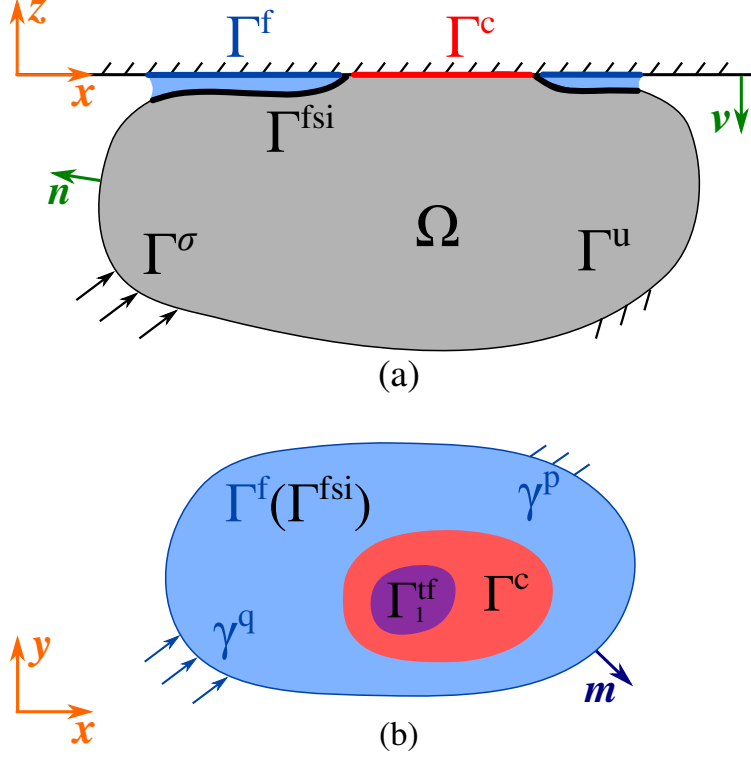


Figure 1: Sketch of the problem under study: (a) contact between a solid and a rigid flat with fluid present in the interface; (b) view of the contact interface. Notations: Γ^c is the active contact zone, Γ^{fsi} is the fluid-structure interface, Γ^f is the lubrication surface where the Reynolds equation is solved (Γ^f is the projection of Γ^{fsi} on the rigid flat), Γ_1^{tf} is a trapped fluid zone.

of the trapped fluid is to be considered separately. We assume here that in the initial configuration $\Gamma^c = \emptyset$ and $n_{\text{tf}} = 0$, so that the fluid flow zone occupies the whole interface. This assumption makes impossible appearance of non-contact zones which do not belong to Γ^{fsi} or one of the trapped fluid zones Γ_i^{tf} in any deformed configuration. However, consideration of such a case (e.g. air bubbles entrapment) could be included into the framework.

2.1 Solid mechanics problem with unilateral contact

The deformation of the solid (in absence of the fluid) is governed by the balance of momentum equation complemented by the contact and boundary conditions:

$$\begin{cases} \nabla \cdot \boldsymbol{\sigma}(\mathbf{u}) = 0 & \text{in } \Omega & (2a) \\ g(\mathbf{u}) \geq 0, \sigma_n(\mathbf{u}) \leq 0, g(\mathbf{u}) \sigma_n(\mathbf{u}) = 0 & \text{on } \Gamma & (2b) \\ \mathbf{u} = \mathbf{u}_0 & \text{on } \Gamma^u & (2c) \\ \boldsymbol{\sigma} \cdot \mathbf{n} = \boldsymbol{\sigma}_0 & \text{on } \Gamma^\sigma & (2d) \end{cases}$$

where $\mathbf{u} = \mathbf{x} - \mathbf{X}$ is the displacement field (\mathbf{x} and \mathbf{X} are the coordinates in the deformed and the initial configurations, respectively), $\boldsymbol{\sigma}$ is the Cauchy stress tensor; (2b) are the Hertz-Signorini-Moreau conditions of the non-adhesive frictionless unilateral contact (Wriggers, 2006; Yastrebov, 2013), $\sigma_n = \mathbf{n} \cdot \boldsymbol{\sigma} \cdot \mathbf{n}$ is the normal traction on the solid's surface (to which \mathbf{n} is the outer normal). We denote by $g(\mathbf{u})$ the normal gap function, i.e. the signed distance between the surface of the solid and the rigid flat: $g > 0$ in case of separation, $g = 0$ in contact and $g < 0$ refers to penetration, which is not admissible:

$$g(\mathbf{u}) = g_0(\mathbf{X}) + \mathbf{u} \cdot \boldsymbol{\nu}, \quad (3)$$

where $g_0(\mathbf{X})$ is the initial gap and $\boldsymbol{\nu}$ is the normal to the rigid flat. Finally, (2c) are the Dirichlet boundary conditions with a prescribed displacement \mathbf{u}_0 and (2d) are the Neumann boundary conditions with a prescribed surface traction $\boldsymbol{\sigma}_0$, defined on $\Gamma^u \subset \partial\Omega$ and $\Gamma^\sigma \subset \partial\Omega$, respectively. Note that here we will consider isotropic

linearly elastic solid, i.e. the Cauchy stress tensor is related to the infinitesimal strain tensor $\boldsymbol{\varepsilon} = (\nabla \mathbf{u})^s$ by the Hooke's law: $\boldsymbol{\sigma} = \lambda \text{trace}(\boldsymbol{\varepsilon}) \mathbf{I} + 2\mu \boldsymbol{\varepsilon}$ with the Lamé constants (elastic moduli) λ and μ , \mathbf{I} is the identity tensor. However, the proposed coupled framework concerns processes occurring in the contact interface only and permits arbitrary constitutive laws for the underlying solid, see examples in Shvarts (2019).

2.2 Thin fluid flow

The thin fluid flow is governed by:

$$\begin{cases} \nabla \cdot [g(\mathbf{u})^3 \nabla p] = 0 & \text{in } \Gamma^f & (4a) \\ p = p_0 & \text{on } \gamma_p & (4b) \\ \mathbf{q} \cdot \mathbf{m} = q_0 & \text{on } \gamma_q & (4c) \end{cases}$$

where (4a) is the Reynolds equation for isoviscous incompressible Newtonian fluid (Hamrock et al., 2004), note that the tangential relative motion of the solid walls is not considered here whereas the normal approaching is assumed to be quasi-static, $p(x, y)$ is the fluid pressure field defined on the lubrication surface Γ^f , which is a projection of the fluid-structure interface Γ^{fsi} on the plane $z = 0$, and the ∇ operator in (4a) is defined as $\nabla(\cdot) := \partial(\cdot)/\partial x \mathbf{e}_x + \partial(\cdot)/\partial y \mathbf{e}_y$. Finally, (4b) are the Dirichlet boundary conditions with a prescribed fluid pressure p_0 and (4c) are the Neumann boundary conditions with a prescribed fluid flux q_0 , defined on $\gamma_p \subset \partial\Gamma^f$ and $\gamma_q \subset \partial\Gamma^f$, respectively (\mathbf{m} is the outer normal to Γ^f), while the fluid flux is given by:

$$\mathbf{q} = -\frac{g^3}{12\mu} \nabla p, \quad (5)$$

where μ is the dynamic viscosity. Note that for each point $(x, y) \in \Gamma^f$ the thickness of the film is computed as the normal gap $g(\mathbf{u})$ of the corresponding point $(x, y, z) \in \Gamma^{\text{fsi}}$.

2.3 Fluid-structure interface

The equilibrium of the solid and fluid tractions on the fluid-structure interface Γ^{fsi} needs to fulfill the following equation:

$$\boldsymbol{\sigma} \cdot \mathbf{n} = -p \mathbf{n} - \frac{g(\mathbf{u})}{2} \nabla p \quad \text{on } \Gamma^{\text{fsi}}, \quad (6)$$

where the first right-hand side term is the normal traction due to the hydrostatic pressure, while the second one is the tangential traction due to viscous shear stresses in the fluid that act on the solid's surface (here, it results from the Poiseuille flow), see (Hamrock et al., 2004) for details. Note that the gradient operator here is defined on the lubrication surface Γ^f , and the second term in (6) is not exactly perpendicular to the outward normal \mathbf{n} to the surface Γ^{fsi} . Nevertheless, this slight inconsistency is justified by the requirement of small slopes of the surface geometry for validity of the Reynolds equation in certain applications, such as the fluid flow through fractures (Brown et al., 1995), and is often accepted in elasto-hydrodynamic lubrication problems, see, for example, (Stupkiewicz, 2009; Stupkiewicz et al., 2016).

Moreover, in derivation of the Reynolds equation (4a) the thickness of the fluid film is assumed to be much smaller than other length scales, and therefore, the term corresponding to the tangential traction in (6) is often neglected in lubrication problems, see e.g. (Stupkiewicz, 2018). However, in application to sealing problems, studies of the elasto-hydrodynamic lubrication regime show a noticeable effect of the shear tractions on the seal's leakage, see (Stupkiewicz and Marciniszyn, 2009). Therefore, for the sake of completeness, we will consider both normal and shear components of the fluid-induced traction in the developed framework.

Note also that we do not need to consider no-slip condition (i.e. zero flow velocity at the fluid-structure boundary), as, for example, in (Farhat et al., 1998), since it is already taken into account in the considered form of the Reynolds equation (4a).

2.4 Trapped fluid zones

The hydrostatic pressure p_i^{tf} , developed in the i -th trapped fluid zone, is applied to the surface of the solid body as the normal traction:

$$\sigma_n = -p_i^{\text{tf}} \quad \text{on } \Gamma_i^{\text{tf}}, \quad i = 1 \dots n_{\text{tf}}. \quad (7)$$

However, the pressure p_i^{tf} is *a priori* unknown, and the behaviour of the trapped fluid is not governed by the Reynolds equation. Furthermore, the pressure developed in such trapped fluid pocket can be considerably

higher than the pressure in the fluid flow, and therefore a model of a *incompressible* fluid becomes inaccurate here, see discussions in (Shvarts and Yastrebov, 2018b). Therefore, we will consider the model of a *compressible* fluid with pressure-dependent bulk modulus $K = K_0 + K_1 p_i^{\text{tf}}$, where K_0 [Pa] and K_1 (dimensionless) are model parameters, which is suitable for fluids typically used in lubrication and sealing applications, see also (Kuznetsov, 1985) for details. According to this model, the pressure of the trapped fluid is a non-linear function of the relative change of its volume:

$$p_i^{\text{tf}} = \left(p_{i0}^{\text{tf}} + \frac{K_0}{K_1} \right) \left(\frac{V_i^{\text{tf}}}{V_{i0}^{\text{tf}}} \right)^{-K_1} - \frac{K_0}{K_1}, \quad (8)$$

where V_i^{tf} is the current volume of fluid in the i -th zone, V_{i0}^{tf} is the volume of the fluid in this zone at the moment when it was formed, and p_{i0}^{tf} is the corresponding initial pressure of this trapped fluid. Therefore, since the behaviour of each trapped fluid zone depends on its own set of initial parameters (V_{i0}^{tf} and p_{i0}^{tf}), it has to be considered separately from others. As was mentioned above, we assume that the fluid occupies the whole free volume between the contacting surfaces. Accordingly, the volume of the fluid in the i -th pool is equal to the volume of the gap between the surface Γ_i^{tf} and the rigid flat:

$$V_i^{\text{tf}} = \int_{\Gamma_i^{\text{tf}}} g(\mathbf{u})(-\mathbf{n} \cdot \boldsymbol{\nu}) d\Gamma, \quad (9)$$

where \mathbf{n} is the outward normal to the surface Γ_i^{tf} , and $\boldsymbol{\nu}$ is the normal to the rigid flat, see Fig. 1.

It is important to note, that the presented problem set-up corresponds to the two-way coupling approach, and therefore not only the displacement field \mathbf{u} depends on the fluid pressure p and vice versa, but also the extent of fluid-flow domain Γ^{f} and trapped fluid zones Γ_i^{tf} may depend on the morphology of the active contact zone, i.e. on the resolution of contact constraints. Additional effort may be necessary for handling edge effects, e.g. enforcing continuity of surface tractions across boundaries between contact and fluid-flow zones $\partial\Gamma^{\text{c}} \cap \partial\Gamma^{\text{fsi}}$, and also between contact and trapped fluid zones $\partial\Gamma^{\text{c}} \cap \partial\Gamma_i^{\text{tf}}$ $i = \overline{1, n_{\text{tf}}}$. Below we will discuss in detail our recipes of partitioning the interface and handling these problems. At the same time, the one-way coupling approach, which neglects the action of the fluid pressure on surface of the solid, can also be considered in the present problem statement if equations (6) and (7) are omitted.

3 Variational formulation

Before presenting the numerical framework, we discuss briefly the variational statement of the coupled problem formulated in the previous section. We start by outlining contribution of each sub-problem to the balance of virtual work and then provide the variational formulation of the coupled problem for both one- and two-way coupling approaches.

3.1 Weak formulation of the solid mechanics problem with contact constraints

The variational statement of the solid mechanics problem with contact constraints (2) is well-known, see e.g. (Kikuchi and Oden, 1988), and consists in finding a function $\mathbf{u} \in \mathbf{K}$:

$$\mathbf{K} = \{ \mathbf{u} \in \mathbf{H}^1(\Omega) \mid \mathbf{u} = \mathbf{u}_0 \text{ on } \Gamma^u, g(\mathbf{u}) \geq 0 \text{ on } \Gamma \}, \quad (10)$$

where $\mathbf{H}^1(\Omega)$ denotes the Sobolev space for vector-valued functions with square integrable derivatives, such that:

$$\int_{\Omega} \boldsymbol{\sigma}(\mathbf{u}) : \nabla \delta \mathbf{u} d\Omega - \int_{\Omega} \mathbf{f}_v \cdot \delta \mathbf{u} d\Omega - \int_{\Gamma^{\sigma}} \boldsymbol{\sigma}_0 \cdot \delta \mathbf{u} d\Gamma + \int_{\Gamma^{\text{c}}} \sigma_n \delta g d\Gamma = 0 \quad \forall \delta \mathbf{u} \in \mathbf{V}, \quad (11)$$

where \mathbf{V} is the space for virtual displacements:

$$\mathbf{V} = \{ \mathbf{v} \in \mathbf{H}^1(\Omega) \mid \mathbf{v} = \mathbf{0} \text{ on } \Gamma^u \}. \quad (12)$$

Note that in (11) we used the variation of the normal gap function $\delta g(\mathbf{u})$, related to the virtual displacement $\delta \mathbf{u}$ as:

$$\delta g(\mathbf{u}) = \frac{\partial g}{\partial \mathbf{u}} \cdot \delta \mathbf{u} = \boldsymbol{\nu} \cdot \delta \mathbf{u}, \quad (13)$$

where $\boldsymbol{\nu}$ is the normal to the rigid flat.

3.2 Weak statement of the fluid flow sub-problem

In order to obtain the weak form of the fluid-flow problem (4), we follow the standard approach to elliptic (e.g. steady-state heat conduction) equations, see e.g. (Zienkiewicz and Taylor, 1977), which results in the following statement: find a scalar field $p \in \mathcal{P}$:

$$\mathcal{P} = \{ p \in H^1(\Gamma^f) \mid p = p_0 \text{ on } \gamma^p \}, \quad (14)$$

such that

$$\int_{\Gamma^f} \frac{g^3}{12\eta} \nabla p \cdot \nabla \delta p \, d\Gamma + \int_{\gamma^q} q_0 \delta p \, d\gamma = 0 \quad \forall \delta p \in \mathcal{Q}, \quad (15)$$

where \mathcal{Q} is the space for scalar virtual functions:

$$\mathcal{Q} = \{ \delta p \in H^1(\Gamma^f) \mid \delta p = 0 \text{ on } \gamma^p \}. \quad (16)$$

3.3 Weak form of the fluid-structure interface balance

We may compute the work of the fluid-induced tractions on the surface Γ^{fsi} (6), corresponding to a virtual displacement $\delta \mathbf{u}$, as:

$$\delta W^{\text{fsi}} = \int_{\Gamma^{\text{fsi}}} \left(-p \mathbf{n} - \frac{g}{2} \nabla p \right) \cdot \delta \mathbf{u} \, d\Gamma, \quad (17)$$

and include it to the balance of the virtual work (11) with the negative sign, since the virtual work of surface tractions has a sign opposite to the one of the work of internal forces. It is also important to bear in mind that the traction vector in (6) and (17) is not known *a priori* and depends on the fluid pressure p , its gradient ∇p and the displacement field \mathbf{u} .

3.4 Virtual work of trapped fluid zones

To capture the effect of the trapped fluid pressure on the solid, we recall the thermodynamic definition of the elementary work done on a system, corresponding to an infinitesimal change of its volume. Following this concept, we compute the virtual work of an i -th trapped pool on the surface of the solid as:

$$\delta W_i^{\text{tf}} = -p_i^{\text{tf}} \delta V_i^{\text{tf}}, \quad (18)$$

where the minus sign is used since an increase of the volume of a trapped pool leads to a decrease of its pressure, and consequently, to a release of the energy of the trapped fluid. Since the volume of the fluid inside a trap V_i is a functional of the displacement field \mathbf{u} as defined by the integral (9), δV_i can be treated as its first variation and computed using the directional derivative:

$$\delta V_i^{\text{tf}} = D V_i^{\text{tf}}(\mathbf{u}) \cdot \delta \mathbf{u} = \left. \frac{dV_i^{\text{tf}}(\mathbf{u} + \epsilon \delta \mathbf{u})}{d\epsilon} \right|_{\epsilon=0}. \quad (19)$$

Therefore, the virtual work of the trapped fluid corresponding to a virtual displacement $\delta \mathbf{u}$ can be expressed as:

$$\delta W_i^{\text{tf}} = - \left[\left(p_{i0}^{\text{tf}} + \frac{K_0}{K_1} \right) \left(\frac{V_i^{\text{tf}}}{V_{i0}^{\text{tf}}} \right)^{-K_1} - \frac{K_0}{K_1} \right] D V_i^{\text{tf}}(\mathbf{u}) \cdot \delta \mathbf{u}, \quad (20)$$

which can now be included into the equation for the virtual work (11), taking into account the contribution of each trapped fluid zone separately.

3.5 Variational formulation of the coupled problem

Combining contributions of the sub-problems outlined above, we provide the variational statement of the coupled problem in the spirit of the monolithic approach (Yang and Laursen, 2009; Stupkiewicz, 2018):

Find $\mathbf{u}(x, y, z) \in \mathbf{K}$ and $p(x, y) \in \mathcal{P}$ such that:

$$G^s(\mathbf{u}, p, \delta \mathbf{u}) = 0, \quad \forall \delta \mathbf{u} \in \mathbf{V}, \quad (21a)$$

$$G^f(p, \mathbf{u}, \delta p) = 0, \quad \forall \delta p \in \mathcal{Q}, \quad (21b)$$

where

$$G^s(\mathbf{u}, p, \delta \mathbf{u}) = \int_{\Omega} \boldsymbol{\sigma}(\mathbf{u}) : \nabla \delta \mathbf{u} \, d\Omega - \int_{\Gamma^\sigma} \boldsymbol{\sigma}_0 \cdot \delta \mathbf{u} \, d\Gamma + \int_{\Gamma^c} \sigma_n \boldsymbol{\nu} \cdot \delta \mathbf{u} \, d\Gamma \quad (22a)$$

$$+ \int_{\Gamma^{\text{fsi}}} \left(p \mathbf{n} + \frac{g(\mathbf{u})}{2} \nabla p \right) \cdot \delta \mathbf{u} \, d\Gamma \quad (22b)$$

$$- \sum_{i=1}^{n_{\text{tf}}} \left[\left(p_{i0}^{\text{tf}} + \frac{K_0}{K_1} \right) \left(\frac{V_i^{\text{tf}}(\mathbf{u})}{V_{i0}^{\text{tf}}} \right)^{-K_1} - \frac{K_0}{K_1} \right] DV_i^{\text{tf}}(\mathbf{u}) \cdot \delta \mathbf{u}; \quad (22c)$$

$$G^f(p, \mathbf{u}, \delta p) = \int_{\Gamma^f} \frac{g^3(\mathbf{u})}{12\eta} \nabla p \cdot \nabla \delta p \, d\Gamma + \int_{\gamma^a} q_0 \delta p \, d\gamma, \quad (22d)$$

The weak problem statement (21)-(22) is valid for the two-way coupling approach, when both sub-problems have impact on each other. The one-way coupling approximation for the problem under study can also be considered upon following modifications: (i) omit the fluid-induced tractions on the surface of the solid (22b), (ii) neglect the effect of trapped fluid zones (22c), and (iii) assume rigid solid walls while solving fluid-flow equation (21b). Therefore, in case of one-way coupling, instead of (21), we shall have the following equations:

$$G^s(\mathbf{u}, \delta \mathbf{u}) = 0, \quad \forall \delta \mathbf{u} \in \mathbf{V}, \quad (23a)$$

$$G^f_{\mathbf{u}}(p, \delta p) = 0, \quad \forall \delta p \in \mathcal{P}. \quad (23b)$$

Note that \mathbf{u} is still required as an input to compute the normal gap, hence we used the subscript “ \mathbf{u} ” for $G^f_{\mathbf{u}}$, however, for any given displacement field \mathbf{u} the fluid sub-problem becomes linear under the one-way coupling approach.

4 Computational framework

In this section we discuss the proposed monolithic finite-element framework for the coupled problem. Similarly to the previous section, we discuss handling of each sub-problem separately, and then we present the monolithic resolution algorithm which combines them. We use here the standard mechanical finite element approach for the numerical simulation of the solid deformation, details of which may be found elsewhere. Note that for brevity the same notations are preserved for discretised entities as were introduced in the continuous problem statement. Furthermore, in order to simplify the discussion and concentrate it on the two-way coupling aspects, we use the small deformations and small rotations assumptions, which is (at least partially) justified by the requirement of small slopes of the roughness profile for the validity of the Reynolds equation in certain applications, see e.g. Brown et al. (1995). Nevertheless, the necessary modifications to take into account large deformations and/or large rotations can be added into presented framework. The development of the proposed scheme was undertaken in the finite-element suite Z-set (Besson and Foerch, 1997; Z-set, 2019).

4.1 Mechanical contact

The solution of the considered coupled problem requires partition of the interface into contact, fluid-flow and, possibly multiple, trapped fluid zones, see (1). In order to make the identification of the interface status self-consistent, it appears natural to associate contact elements with faces of the surface Γ , i.e. adopt the “face-to-rigid-surface” discretization approach, rather than the “node-to-rigid-surface” technique, which associates each contact element with a single node of the surface Γ , see (Wriggers, 2006; Konyukhov and Schweizerhof, 2012; Yastrebov, 2013) for more details.

Furthermore, for each point on the surface Γ we consider the interpolation of the gap and of the normal traction as, respectively:

$$g = \sum_{i=1}^m N_i g_i, \quad \sigma_n = \sum_{i=1}^m N_i \sigma_{ni}, \quad (24)$$

where g_i is the nodal gap value, σ_{ni} is the nodal value of the contact pressure (treatment of which is method-dependent and will be discussed in detail below), N_i is the shape function associated with the node i , and m is the total number of nodes on surface Γ , see Fig. 2. Note that the same shape functions are

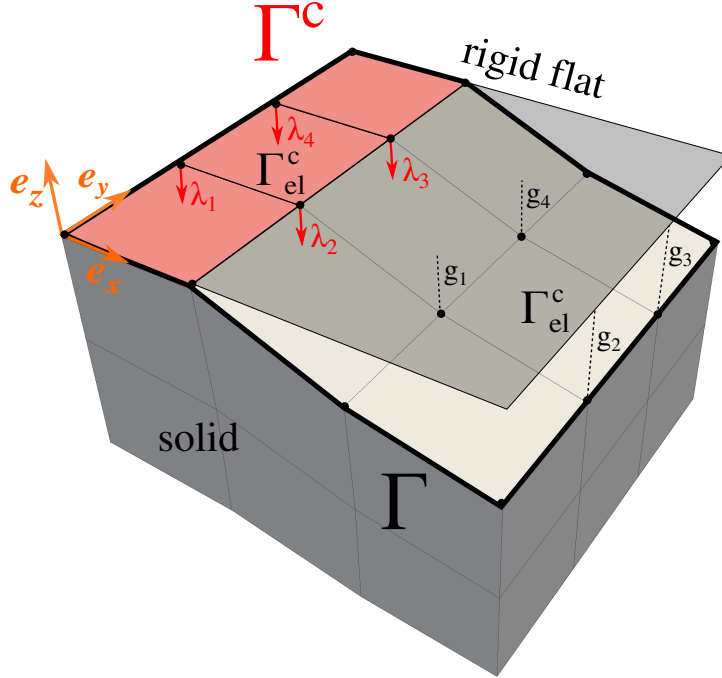


Figure 2: Sketch of the interface highlighting contact elements: Γ is the potential contact zone, Γ^c is the active contact zone (*active set*), Γ_{el}^c is a face associated to one contact element, λ is the Lagrange multiplier, which represents contact pressure and is attributed to each node of the surface Γ , g is the gap function: $g = 0$ on Γ^c and $g > 0$ on $\Gamma \setminus \Gamma^c$.

used here for interpolation of geometric gap and surface tractions, however, it is not a necessary condition. We used bilinear shape functions associated with quadrilateral faces of the discretised surface, nonetheless, polynomials of higher order can be utilized, see Puso et al. (2008).

In case of the considered interpolation (24) contact constraints (2b) cannot be satisfied point-wise on the surface Γ . To overcome this inconsistency, we follow the mortar approach (Puso, 2004; Puso and Laursen, 2004) and consider the third condition in (2b) in the integral form over the surface Γ :

$$\int_{\Gamma} \sigma_n g \, d\Gamma = 0. \quad (25)$$

Substituting (24) into (25) and considering two first conditions of (2b) at every node of the surface Γ , we obtain the following discrete (nodal) form of the contact conditions:

$$\tilde{g}_i \geq 0, \quad \sigma_{ni} \leq 0, \quad \sigma_{ni} \tilde{g}_i = 0, \quad 1 \leq i \leq m, \quad (26)$$

where \tilde{g}_i is termed as the integral (weighted) gap associated with node i and is given by:

$$\tilde{g}_i = \sum_{j=1}^m g_j \int_{\Gamma} N_i N_j \, d\Gamma. \quad (27)$$

In order to solve the contact problem with constraints (26), we use the augmented Lagrangian method, which combines benefits of the classic Lagrange multipliers method (exact satisfaction of the constraints) and the penalty method (so-called “active set strategy” is not required), see also (Alart and Curnier, 1991; Cavalieri and Cardona, 2013). Thus, we append Lagrange multipliers λ_i , $i = 1 \dots m$ to each node of the surface Γ , see Fig. 2, and introduce the following augmented Lagrangian functional:

$$\mathcal{L}^a(\mathbf{U}, \mathbf{L}) = \Pi^s(\mathbf{U}) + W^c(\mathbf{U}, \mathbf{L}), \quad (28)$$

where Π^s is the potential energy of deformed solid, while W^c represents the “potential energy” of the contact and is given by:

$$W^c(\mathbf{U}, \mathbf{L}) = \sum_{i=1}^m \begin{cases} \lambda_i \tilde{g}_i + \frac{\epsilon}{2} \tilde{g}_i^2, & \text{if } \hat{\lambda}_i \leq 0, \\ -\frac{1}{2\epsilon} \lambda_i^2, & \text{if } \hat{\lambda}_i > 0, \end{cases} \quad (29)$$

where ϵ is the so-called augmentation parameter. The following notation of the augmented Lagrange multiplier is introduced: $\hat{\lambda}_i = \lambda_i + \epsilon \tilde{g}_i$, the sign of which defines the contact state of the node: if $\hat{\lambda}_i \leq 0$ the node belongs to the active contact zone, while if $\hat{\lambda}_i > 0$ the node is not in contact. Once the solution is obtained, values of Lagrange multipliers λ_i are equal to respective nodal values of the contact pressure σ_{ni} . In formulas (28)-(29) we denote by $\mathbf{U} = [\mathbf{u}_1, \mathbf{u}_2, \dots, \mathbf{u}_m]^\top$ and $\mathbf{L} = [\lambda_1, \lambda_2, \dots, \lambda_m]^\top$ vectors of nodal displacements and values of Lagrange multipliers, respectively.

The solution of the contact problem is equivalent to the stationary saddle point of the Lagrangian (28), at which its variation vanishes:

$$\delta \mathcal{L}^a(\mathbf{U}, \mathbf{L}) = \delta \Pi^s(\mathbf{U}) + \frac{\partial W^c(\mathbf{U}, \mathbf{L})}{\partial \mathbf{U}} \cdot \delta \mathbf{U} + \frac{\partial W^c(\mathbf{U}, \mathbf{L})}{\partial \mathbf{L}} \delta \mathbf{L} = 0, \quad (30)$$

where the virtual work of the internal forces is expressed using the directional derivative:

$$\delta \Pi^s(\mathbf{U}) = D \Pi^s(\mathbf{U}) \cdot \delta \mathbf{U} = \left. \frac{d \Pi^s(\mathbf{U} + \gamma \delta \mathbf{U})}{d\gamma} \right|_{\gamma=0}, \quad (31)$$

while the second terms in (30) is equivalent to the virtual work of contact forces, cf. (22a), and the third term in (30) ensures that $\tilde{g}_i = 0$ in the active contact zone. In order to derive the contribution of each contact element to the balance of virtual work and determine the element's status (independently from the neighbouring elements) we compute the integral gap (27) over the face Γ_{el} associated with each contact element:

$$\tilde{g}_i = \sum_{j=1}^n g_j \int_{\Gamma_{el}} N_i N_j d\Gamma_{el} = \sum_{j=1}^n g_j I_{ij}, \quad (32)$$

where n is the total number of nodes of the face Γ_{el} . The weights I_{ij} are calculated as:

$$I_{ij} = \int_{-1}^1 \int_{-1}^1 N_i N_j J d\xi d\eta, \quad (33)$$

where J is the Jacobian of the transformation of the physical coordinates $\mathbf{x} = (x, y, z)$ on the surface Γ_{el} to the face's coordinates in the parent space $\boldsymbol{\xi} = (\xi, \eta)$:

$$J = \left| \frac{\partial \mathbf{x}}{\partial \xi} \times \frac{\partial \mathbf{x}}{\partial \eta} \right|, \quad \mathbf{x} = \sum_{i=1}^n \mathbf{x}_i N_i \quad (34)$$

where \mathbf{x}_i is the position of the i -th node of the face. Using the Gauss quadrature rules, the integral in (33) is computed as:

$$I_{ij} = \sum_{k=1}^{n_{gp}} w_k N_i(\boldsymbol{\xi}_k) N_j(\boldsymbol{\xi}_k) J(\boldsymbol{\xi}_k) \quad (35)$$

where n_{gp} is the number of Gauss points associated with the face Γ_{el} , w_k is the weight coefficient of the k -th Gauss point, and $\boldsymbol{\xi}_k$ are its coordinates in the parent space.

In order to find the contribution of each contact element to the balance of virtual works, we calculate the variation of (29):

$$\delta W_{el}^c = \sum_{i=1}^n \begin{cases} \hat{\lambda}_i \sum_{j=1}^n I_{ij} \frac{\partial g_j}{\partial \mathbf{u}_j} \delta \mathbf{u}_j + \tilde{g}_i \delta \lambda_i, & \hat{\lambda}_i \leq 0 \\ -\frac{1}{\epsilon} \lambda_i \delta \lambda_i, & \hat{\lambda}_i > 0 \end{cases} \quad (36)$$

where \mathbf{u}_j is the displacement vector of the node j . Note that in accordance with the infinitesimal strain formulation the Jacobian is not varied. We shall term hereinafter an element as active if at least at one of its nodes $\hat{\lambda}_i \leq 0$, $i = 1 \dots n$, and inactive otherwise.

In order to perform linearisation of the problem, we calculate the second variation of the virtual work $\delta W_{\text{el}}^{\text{c}}$:

$$\Delta \delta W_{\text{el}}^{\text{c}} = \sum_{i=1}^n \begin{cases} \epsilon \sum_{j=1}^n I_{ij} \frac{\partial g_j}{\partial \mathbf{u}_j} \delta \mathbf{u}_j + \sum_{k=1}^n I_{ik} \frac{\partial g_k}{\partial \mathbf{u}_k} \Delta \mathbf{u}_k + \sum_{j=1}^n I_{ij} \frac{\partial g_j}{\partial \lambda_j} (\delta \mathbf{u}_j \Delta \lambda_i + \Delta \mathbf{u}_j \delta \lambda_i), & \hat{\lambda}_i \leq 0 \\ -\frac{1}{\epsilon} \delta \lambda_i \Delta \lambda_i, & \hat{\lambda}_i > 0. \end{cases} \quad (37)$$

Finally, the virtual work (36) and its variation (37) could be expressed in a compact form, introducing the residual vector \mathbf{R}^{c} and the tangent matrix \mathbf{K}^{c} of a contact element:

$$\delta W_{\text{el}}^{\text{c}} = \underbrace{\begin{bmatrix} \mathbf{R}_{\mathbf{u}}^{\text{c}} \\ \mathbf{R}_{\lambda}^{\text{c}} \end{bmatrix}}_{\mathbf{R}^{\text{c}}}^{\text{T}} \begin{bmatrix} \delta \mathbf{u} \\ \delta \lambda \end{bmatrix}, \quad \Delta \delta W_{\text{el}}^{\text{c}} = \begin{bmatrix} \Delta \mathbf{u} \\ \Delta \lambda \end{bmatrix}^{\text{T}} \underbrace{\begin{bmatrix} \mathbf{K}_{\mathbf{u}\mathbf{u}}^{\text{c}} & \mathbf{K}_{\mathbf{u}\lambda}^{\text{c}} \\ \mathbf{K}_{\lambda\mathbf{u}}^{\text{c}} & \mathbf{K}_{\lambda\lambda}^{\text{c}} \end{bmatrix}}_{\mathbf{K}^{\text{c}}} \begin{bmatrix} \delta \mathbf{u} \\ \delta \lambda \end{bmatrix}, \quad (38)$$

where for brevity we use the notations $\delta \mathbf{u} = [\delta \mathbf{u}_1, \dots, \delta \mathbf{u}_n]^{\text{T}}$, $\Delta \mathbf{u} = [\Delta \mathbf{u}_1, \dots, \Delta \mathbf{u}_n]^{\text{T}}$ and $\delta \lambda = [\delta \lambda_1, \dots, \delta \lambda_n]^{\text{T}}$, $\Delta \lambda = [\Delta \lambda_1, \dots, \Delta \lambda_n]^{\text{T}}$. Ready-to-implement expressions of the outlined components of \mathbf{R}^{c} and \mathbf{K}^{c} are given in the Appendix A.1.

The residual vector \mathbf{R}^{c} and tangent matrix \mathbf{K}^{c} are updated on each iteration of the Newton-Raphson method and added to the corresponding entries of the global residual vector and tangent matrix. Note that in the frictionless case considered here the tangent matrix of the contact element is symmetric, i.e. $\mathbf{K}_{\mathbf{u}\lambda}^{\text{c}} = \mathbf{K}_{\lambda\mathbf{u}}^{\text{c}}$.

4.1.1 Post-processing computation of the real contact area

The presented above contact element formulation is sufficient for resolution of the contact constraints (26). However, during the post-processing stage, different methods may be applied to compute the real contact area. A possible straightforward approach is to sum up areas A_{el} of faces Γ_{el} associated with active elements, i.e. the ones that have at least one node with $\hat{\lambda}_i \leq 0$ (dashed areas in Fig. 3):

$$A_{\text{el}} = \begin{cases} \sum_{k=1}^{n_{\text{gp}}} w_k J(\boldsymbol{\xi}_k), & \exists i \in [1, \dots, n] : \hat{\lambda}_i \leq 0 \\ 0, & \forall i \in [1, \dots, n] : \hat{\lambda}_i > 0, \end{cases} \quad (39)$$

where n is the number of nodes of the contact element, n_{gp} is the number of Gauss points associated with the face Γ_{el} , w_k is the weight coefficient of the k -th Gauss point, and $\boldsymbol{\xi}_k$ are its coordinates in the parent space.

However, our study showed that this method of computation of the contact area leads to its significant overestimation. We propose here a more precise approach to computing of the contact area: considering separately each contact element, only if $\hat{\lambda}_i \leq 0$ at a node i , we add up to the contact area contribution from

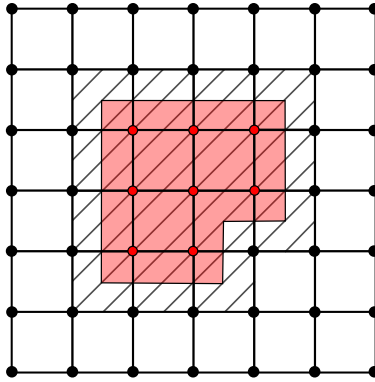


Figure 3: Sketch on the computation of the real contact area. Red circles represent nodes with $\hat{\lambda}_i \leq 0$, black ones correspond to $\hat{\lambda}_i > 0$. The dashed area represents the contact area computed by summing up areas of all active elements, see (39). The shaded area is obtained by a refined approach of summing up areas corresponding to nodes with $\hat{\lambda}_i \leq 0$, computed using the nearest Gauss point to node i , see (40).

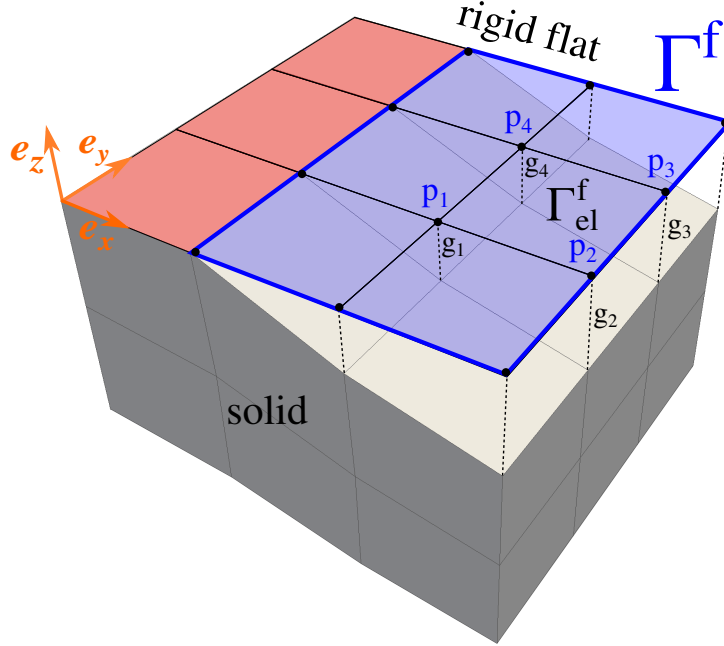


Figure 4: Sketch of the interface highlighting fluid flow elements: Γ^f is the lubrication surface (plane $z = 0$), where the Reynolds equation is defined, Γ_{el}^f is a face on this surface associated to one fluid flow element, p is the fluid pressure DOF, added to each node of the surface of the solid (note that the constant fluid pressure across the film thickness is assumed).

the Gauss point closest to this node (shaded area in Fig. 3):

$$A_{el} = \sum_{i=1}^n \begin{cases} w_i J(\xi_i), & \hat{\lambda}_i \leq 0 \\ 0, & \hat{\lambda}_i > 0, \end{cases} \quad (40)$$

where w_i and ξ_i are the weight coefficient and the position of a Gauss point closest to the node i . Note that we assumed here that n (the number of element's nodes where Lagrange multipliers λ_i are considered) equals to n_{gp} (the number of Gauss points of the corresponding face). However, it might not be the case if, for example, shape functions of different order are used for interpolation of the geometry and of the contact pressure, cf. (24), see also (Puso et al., 2008), and a different refined approach of the real contact area computation will be required. The comparison of two discussed approaches to real contact area computation will be presented below.

4.2 Thin fluid flow

Next, we discuss the implementation of the weak form of the fluid flow problem, see (21b), into the finite-element framework. In order to concentrate the reader's attention on the aspects of the coupling, we assume that the prescribed fluid flux $q_0 = 0$ on $\gamma^q \subset \partial\Gamma^f$, however, a non-trivial Neumann boundary condition could be included in the present formulation in the standard manner.

Following the assumption of the constant fluid pressure across the film thickness, we attribute a fluid pressure DOF to each node of the surface Γ and define a finite element for the fluid transport problem for each face of the surface Γ^f , formed by faces of Γ^{fsi} projected on the rigid flat, see Fig. 4. We use the same interpolation for the gap as in the contact problem, see (24), while for the fluid pressure p and the "test" function δp we also have:

$$p = \sum_{i=1}^n N_i p_i, \quad \delta p = \sum_{i=1}^n N_i \delta p_i, \quad (41)$$

where n is the number of nodes which belong to an element. Substituting these expressions into (22d) we obtain the following contribution of one fluid-flow element to the balance of the virtual work:

$$\delta W_{\text{el}}^f = \sum_{i=1}^n \delta p_i \int_{-1}^1 \int_{-1}^1 \left(\sum_{k=1}^n N_k g_k \right)^3 \left(\mathbf{J}^{-1} \sum_{j=1}^n \nabla N_j p_j \right) (\mathbf{J}^{-1} \nabla N_i) \det(\mathbf{J}) d\xi d\eta, \quad (42)$$

where (ξ, η) are coordinates in the parent space, \mathbf{J} is the Jacobian matrix defined as:

$$\mathbf{J} = \begin{bmatrix} \frac{\partial x}{\partial \xi} & \frac{\partial x}{\partial \eta} \\ \frac{\partial y}{\partial \xi} & \frac{\partial y}{\partial \eta} \end{bmatrix} \quad (43)$$

and $\det(\mathbf{J})$ is its determinant. The second variation, required for the linearisation of the coupled problem, reads:

$$\begin{aligned} \Delta \delta W_{\text{el}}^f &= \sum_{i=1}^n \delta p_i \left\{ \sum_{j=1}^n \Delta p_j \int_{-1}^1 \int_{-1}^1 \left(\sum_{k=1}^n N_k g_k \right)^3 (\mathbf{J}^{-1} \nabla N_j) (\mathbf{J}^{-1} \nabla N_i) \det(\mathbf{J}) d\xi d\eta \right. \\ &\quad \left. + \sum_{l=1}^n \frac{\partial g_l}{\partial \mathbf{u}_l} \Delta \mathbf{u}_l \int_{-1}^1 \int_{-1}^1 3 \left(\sum_{k=1}^n N_k g_k \right)^2 N_l \left(\mathbf{J}^{-1} \sum_{j=1}^n \nabla N_j p_j \right) (\mathbf{J}^{-1} \nabla N_i) \det(\mathbf{J}) d\xi d\eta \right\}. \quad (44) \end{aligned}$$

Note that the variation of the Jacobian matrix \mathbf{J} is not considered due to assumptions of small deformations and small rotations.

Introducing the residual vector \mathbf{R}^f and the tangent matrix \mathbf{K}^f of a fluid flow element (explicitly given in Appendix A.2), we may write:

$$\delta W_{\text{el}}^f = \begin{bmatrix} \mathbf{R}_p^f \\ 0 \end{bmatrix}^T \begin{bmatrix} \delta p \\ \delta \mathbf{u} \end{bmatrix}, \quad \Delta \delta W_{\text{el}}^f = \begin{bmatrix} \Delta p \\ \Delta \mathbf{u} \end{bmatrix}^T \begin{bmatrix} \mathbf{K}_{pp}^f & 0 \\ \mathbf{K}_{\mathbf{u}p}^f & 0 \end{bmatrix} \begin{bmatrix} \delta p \\ \delta \mathbf{u} \end{bmatrix}, \quad (45)$$

with $\delta p = [\delta p_1, \dots, \delta p_n]^T$ and similarly $\Delta p = [\Delta p_1, \dots, \Delta p_n]^T$. Note the presented formulation of the fluid-flow element was derived for the two-way coupled problem, however, it is also suitable for the one-way coupling. The only required modification is the assumption of the rigid walls of the solid, according to which the variation of the virtual work with respect to the displacement in (44) vanishes and consequently $\mathbf{K}_{\mathbf{u}p}^f = 0$.

4.3 Fluid-structure interface

To include the virtual work of fluid tractions on the solid's surface (22b) into the numerical framework, we associate a fluid-structure interface element with each face of the surface Γ^{fsi} , see Fig. 5. We use the same interpolation of the fluid pressure and the gap, as in (41) and (24), respectively. Therefore, the contribution of each fluid-structure interface element to the balance of virtual work reads:

$$\delta W_{\text{el}}^{\text{fsi}} = \sum_{i=1}^n \delta \mathbf{u}_i \left\{ \sum_{j=1}^n p_j \int_{-1}^1 \int_{-1}^1 \mathbf{n} N_i N_j J d\xi d\eta + \frac{1}{2} \sum_{k=1}^n g_k \int_{-1}^1 \int_{-1}^1 \left(\mathbf{J}^{-1} \sum_{l=1}^n \nabla N_l p_l \right) N_i N_k J d\xi d\eta \right\}, \quad (46)$$

where the gradients of shape functions ∇N_l are computed on the projection of the face Γ^{fsi} on the rigid flat, i.e. in the same sense as in Subsection 4.2. The corresponding Jacobian matrix \mathbf{J} was defined in (43), and the normal \mathbf{n} is given by:

$$\mathbf{n} = \frac{\frac{\partial \mathbf{x}}{\partial \xi} \times \frac{\partial \mathbf{x}}{\partial \eta}}{\left| \frac{\partial \mathbf{x}}{\partial \xi} \times \frac{\partial \mathbf{x}}{\partial \eta} \right|}, \quad \mathbf{x} = \sum_{i=1}^n \mathbf{x}_i N_i. \quad (47)$$

Note that here J is not $\det(\mathbf{J})$, but is computed as in (34). The second variation then takes the following form:

$$\begin{aligned} \Delta \delta W_{\text{el}}^{\text{fsi}} &= \sum_{i=1}^n \delta \mathbf{u}_i \left\{ \sum_{j=1}^n \Delta p_j \int_{-1}^1 \int_{-1}^1 \mathbf{n} N_i N_j J d\xi d\eta + \frac{1}{2} \sum_{k=1}^n \frac{\partial g_k}{\partial \mathbf{u}_k} \Delta \mathbf{u}_k \int_{-1}^1 \int_{-1}^1 \left(\mathbf{J}^{-1} \sum_{l=1}^n \nabla N_l p_l \right) N_i N_k J d\xi d\eta \right. \\ &\quad \left. + \frac{1}{2} \sum_{k=1}^n g_k \sum_{l=1}^n \Delta p_l \int_{-1}^1 \int_{-1}^1 (\mathbf{J}^{-1} \nabla N_l) N_i N_k J d\xi d\eta \right\}, \quad (48) \end{aligned}$$

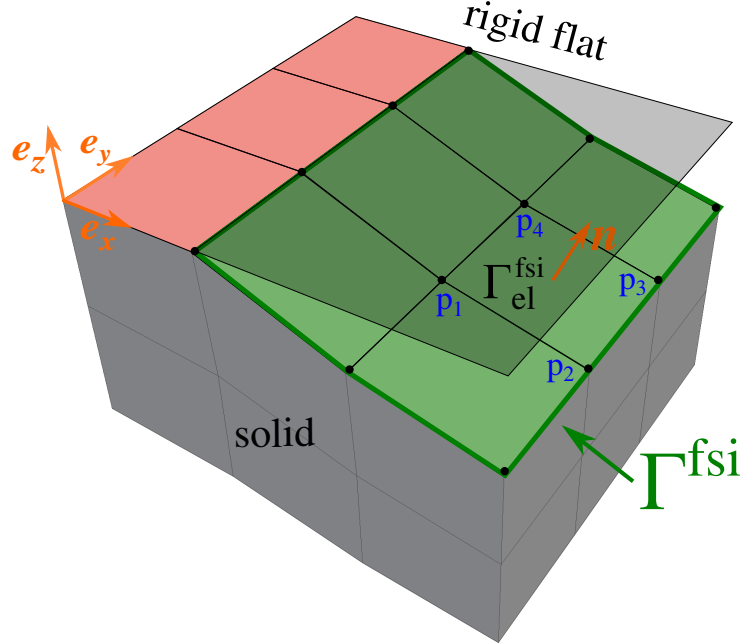


Figure 5: Sketch of the interface highlighting FSI elements: Γ^{fsi} is fluid-structure interface on the surface of the solid, $\Gamma_{\text{el}}^{\text{fsi}}$ is a face associated to one FSI element, p is the fluid pressure at each node of this surface and \mathbf{n} is the outer normal.

where variations of the Jacobian J , the matrix \mathbf{J} and the normal vector \mathbf{n} are not considered due to assumptions of small deformations and small rotations.

Finally, the associated virtual work and its variation could be expressed in a compact form using the residual vector \mathbf{R}^{fsi} and the tangent matrix \mathbf{K}^{fsi} of a FSI element (details can be found in Appendix A.3):

$$\delta W_{\text{el}}^{\text{fsi}} = \begin{bmatrix} \mathbf{R}_{\mathbf{u}}^{\text{fsi}} \\ 0 \end{bmatrix}^T \begin{bmatrix} \delta \mathbf{u} \\ \delta p \end{bmatrix}, \quad \Delta \delta W_{\text{el}}^{\text{fsi}} = \begin{bmatrix} \Delta \mathbf{u} \\ \Delta p \end{bmatrix}^T \begin{bmatrix} \mathbf{K}_{\mathbf{uu}}^{\text{fsi}} & 0 \\ \mathbf{K}_{p\mathbf{u}}^{\text{fsi}} & 0 \end{bmatrix} \begin{bmatrix} \delta \mathbf{u} \\ \delta p \end{bmatrix}. \quad (49)$$

Note that in case of one-way coupling the action of the fluid pressure on the surface of the solid is neglected, so that the virtual work (22b) vanishes and no contribution of the FSI element is included into the global system, i.e. $\mathbf{R}_{\mathbf{u}}^{\text{fsi}} = 0$, $\mathbf{K}_{\mathbf{uu}}^{\text{fsi}} = \mathbf{K}_{p\mathbf{u}}^{\text{fsi}} = 0$.

4.4 Trapped fluid zones

In order to take into account the effect of pressurized volumes of trapped fluid (22c) on the coupled problem, we follow (Shvarts and Yastrebov, 2018b) and use the nonlinear penalty method to simulate the behaviour of the compressible fluid with a pressure-dependent bulk modulus. We discuss here two possible approaches for implementing this model into the finite-element framework. First, we present a “super-element” formulation for a trapped-fluid element containing all faces of one trapped fluid zone $\Gamma_i^{\text{tf}}, i = \overline{1, n_{\text{tf}}}$. A possible standard finite-element formulation which computes contributions from each face of the trapped fluid zone separately is also stated, and benefits and drawbacks of these two approaches are briefly discussed.

4.4.1 “Super-element” formulation

In the finite-element framework the volume of the gap (9) can be calculated by the following formula:

$$V_i^{\text{tf}}(\mathbf{U}) = \sum_{k=1}^{m_i} \int_{-1}^1 \int_{-1}^1 \sum_{j=1}^{n_k} g(\mathbf{u}_j) N_j(\xi, \eta) (-\mathbf{n}_k \cdot \boldsymbol{\nu}) J d\xi d\eta, \quad (50)$$

where the summation with respect to index $k = \overline{1, m_i}$ is performed over all faces of the surface Γ_i^{tf} , and the summation with respect to $j = \overline{1, n_k}$ is over all nodes of the k -th face. Thus, we denote by

$\mathbf{U} = [\mathbf{u}_1, \dots, \mathbf{u}_j, \dots, \mathbf{u}_M]^\top$ vector of displacements of all M nodes on the surface Γ_i^{tf} , which shall serve as the DOF vector for the trapped fluid “super-element”. Next, $g(\mathbf{u}_j)$ is the normal gap computed for the j -th node of the k -th face and $N_j(\xi, \eta)$ is the shape function associated with this node; $\boldsymbol{\xi} = (\xi, \eta)$ are coordinates in the parent space, and J is the Jacobian defined in (34). Finally, \mathbf{n}_k is the normal to the k -th face, which can be computed in the same way as in (47). The integral in (50) can be calculated using the Gauss quadrature rule as:

$$V_i^{\text{tf}}(\mathbf{U}) = \sum_{k=1}^{m_i} \sum_{l=1}^{n_k^{\text{gp}}} \sum_{j=1}^{n_k} g(\mathbf{u}_j) N_j(\boldsymbol{\xi}_l) (-\mathbf{n}_k(\boldsymbol{\xi}_l) \cdot \boldsymbol{\nu}) J(\boldsymbol{\xi}_l) w_l, \quad (51)$$

where n_k^{gp} is the number of Gauss points associated with the k -th face of the surface Γ_i^{tf} , w_l is the weight coefficient of the l -th Gauss point, $\boldsymbol{\xi}_l$ are its coordinates in the parent space.

Therefore, using the expression for the virtual work (20), we may write the residual vector and the tangent matrix for the trapped fluid “super-element” as:

$$\begin{aligned} \mathbf{R}_{\mathbf{u}}^{\text{tf}_i} &= - \left\{ \left(\frac{K_0}{K_1} + p_0^{\text{tf}} \right) \left(\frac{V_i^{\text{tf}}(\mathbf{U})}{V_0^{\text{tf}}} \right)^{-K_1} - \frac{K_0}{K_1} \right\} \left[\frac{\partial V_i^{\text{tf}}(\mathbf{U})}{\partial \mathbf{U}} \right], \\ \mathbf{K}_{\mathbf{uu}}^{\text{tf}_i} &= \left(\frac{K_0}{K_1} + p_0^{\text{tf}} \right) \frac{K_1}{V_0^{\text{tf}}} \left(\frac{V_i^{\text{tf}}(\mathbf{U})}{V_0^{\text{tf}}} \right)^{-K_1-1} \left[\frac{\partial V_i^{\text{tf}}(\mathbf{U})}{\partial \mathbf{U}} \right] \otimes \left[\frac{\partial V_i^{\text{tf}}(\mathbf{U})}{\partial \mathbf{U}} \right]^\top, \end{aligned} \quad (52)$$

where \otimes is the tensor product. Note that we used the small strain formulation and neglected the variation of normals, and therefore the matrix of second derivatives $\partial^2 V_i^{\text{tf}} / \partial \mathbf{U}^2$ is zero, which simplifies the formulation of $\mathbf{K}_{\mathbf{uu}}^{\text{tf}_i}$.

4.4.2 Standard finite-element formulation

Alternatively to the “super-element” formulation presented above, the standard finite-element formulation can be used, according to which the residual vector $\mathbf{R}_{\mathbf{u}}^{\text{tf}_i}$ and the tangent matrix $\mathbf{K}_{\mathbf{uu}}^{\text{tf}_i}$ are constructed using separate contributions from each face of the trapped fluid zone. However, in application to the considered problem the standard approach is bound to certain limitations, which will be discussed below.

Indeed, the volume of the gap (50) can be computed as sum of volumes V_k^{tf} corresponding to each single face:

$$V_i^{\text{tf}}(\mathbf{U}) = \sum_{k=1}^{m_i} V_k^{\text{tf}}(\mathbf{U}_k), \quad V_k^{\text{tf}}(\mathbf{U}_k) = \int_{-1}^1 \int_{-1}^1 \sum_{j=1}^{n_k} g_n(\mathbf{u}_j) N_j(\xi, \eta) (-\mathbf{n}_k \cdot \boldsymbol{\nu}) J d\xi d\eta, \quad (53)$$

where \mathbf{U}_k is the vector of displacements of nodes of the k -th face only. However, the tangent matrix $\mathbf{K}_{\mathbf{uu}}^{\text{tf}_i}$ includes the tensor product $[\partial V_i^{\text{tf}} / \partial \mathbf{U}] \otimes [\partial V_i^{\text{tf}} / \partial \mathbf{U}]^\top$, see (52), and therefore is not sparse and cannot be constructed using the standard assembly process, combining contribution from each face separately.

Nevertheless, the standard finite-element formulation can still be used to handle the trapped fluid model, if the method of the Lagrange multiplier and the penalty method are used simultaneously. In order to show that, following (Abaqus 2018, 2018), we consider the contribution of the trapped fluid to the combined Lagrangian for the coupled problem as:

$$W_i^{\text{tf}} = -\lambda_i^{\text{tf}} \left[V_i^{\text{tf}}(\mathbf{U}) - V_i^{\text{tf}*}(p_i^{\text{tf}}) \right], \quad (54)$$

where λ_i^{tf} is an additional Lagrange multiplier, $V_i^{\text{tf}}(\mathbf{U})$ is computed in the same sense as in (9), while $V_i^{\text{tf}*}(p_i^{\text{tf}})$ represents the volume of the trapped fluid as a function of its pressure, i.e. the inverse of the constitutive relation (8):

$$V_i^{\text{tf}*}(p_i^{\text{tf}}) = V_{i0}^{\text{tf}} \left(\frac{p_i^{\text{tf}} + K_0/K_1}{p_{i0}^{\text{tf}} + K_0/K_1} \right)^{-1/K_1}. \quad (55)$$

Substituting p_i^{tf} by λ_i^{tf} in (55), we may express the variation of the term W_i^{tf} as:

$$\delta W_i^{\text{tf}} = - \left[\lambda_i^{\text{tf}} \frac{\partial V_i^{\text{tf}}(\mathbf{U})}{\partial \mathbf{U}} \cdot \delta \mathbf{U} + \left(V_i^{\text{tf}}(\mathbf{U}) - V_i^{\text{tf}*}(\lambda_i^{\text{tf}}) \right) \delta \lambda_i^{\text{tf}} - \lambda_i^{\text{tf}} \frac{\partial V_i^{\text{tf}*}(\lambda_i^{\text{tf}})}{\partial \lambda_i^{\text{tf}}} \delta \lambda_i^{\text{tf}} \right], \quad (56)$$

which permits now to avoid the tensor product in the tangent matrix $\mathbf{K}_{\mathbf{uu}}^{\text{tf}_i}$ and apply the standard finite-element assembly, combining contribution from each face separately by using (53).

Furthermore, if a problem under consideration involves multiple trapped fluid zones, then an additional Lagrange multiplier λ_i^{tf} needs to be considered for each one of them. However, the number and the extent of trapped fluid zones can vary not only between load steps, but also between iterations of the Newton-Raphson method. The associated inevitable change of the size of the global DOF vector, and consequently, the global matrix, is undesirable, particularly for an implicit finite-element code, and moreover, can make the algorithm for tracking trapped fluid zones (discussed below) more complex. Therefore, in our implementation we followed the proposed above approach of the “super-element” for each trapped fluid zone, which does not require additional DOFs. Nevertheless, it is important to bear in mind that in this latter case the tangent matrix of the trapped fluid element is not sparse, which could increase the storage space required for the construction of the global matrix, as well as its bandwidth.

4.5 Monolithic coupling

We have discussed contribution of all sub-problems to the balance of virtual works and formulation of the residual vectors and tangent matrices for the respective elements. Therefore, following the monolithic approach, we combine now these contributions together, outlining the general structure of the global tangent matrix and residual vector, constructed for each iteration of the Newton-Raphson method. Moreover, we propose a novel algorithm for identification of the local status of the interface in the sense of (1).

4.5.1 The global residual vector and tangent matrix for the coupled problem

We will denote here by $\mathbf{v} = [\mathbf{u}; \lambda, p]^T$ the global vector of the nodal DOFs, consisting of displacement components, Lagrange multipliers for the contact problem and fluid pressure values for the fluid flow problem. Note that the trapped fluid elements do not require any additional degrees of freedom, since the penalty method was used. Furthermore, by $\Delta \mathbf{v} = [\Delta \mathbf{u}; \Delta \lambda, \Delta p]^T$ we shall denote the increment of the DOF vector, corresponding to one iteration. Then the global system of equations takes the following form.

$$\begin{bmatrix} \mathbf{K}_{\mathbf{uu}}^* & \mathbf{K}_{\mathbf{u}\lambda}^c & \mathbf{K}_{\mathbf{u}p}^f \\ \mathbf{K}_{\lambda\mathbf{u}}^c & \mathbf{K}_{\lambda\lambda}^c & 0 \\ \mathbf{K}_{p\mathbf{u}}^{\text{fsi}} & 0 & \mathbf{K}_{pp}^f \end{bmatrix} \begin{bmatrix} \Delta \mathbf{u} \\ \Delta \lambda \\ \Delta p \end{bmatrix} = \begin{bmatrix} \mathbf{R}_{\mathbf{u}}^* \\ \mathbf{R}_{\lambda}^c \\ \mathbf{R}_p^f \end{bmatrix}, \quad (57)$$

The matrix $\mathbf{K}_{\mathbf{uu}}^*$ and vector $\mathbf{R}_{\mathbf{u}}^*$ are assembled using corresponding entities of all aforementioned sub-problems, introduced in (38), (45), (49) and (52):

$$\mathbf{K}_{\mathbf{uu}}^* = \mathbf{K}_{\mathbf{uu}}^s + \mathbf{K}_{\mathbf{uu}}^c + \mathbf{K}_{\mathbf{uu}}^{\text{fsi}} + \sum_{i=1}^{n_{\text{tf}}} \mathbf{K}_{\mathbf{uu}}^{\text{tf}_i}, \quad \mathbf{R}_{\mathbf{u}}^* = \mathbf{R}_{\mathbf{u}}^s + \mathbf{R}_{\mathbf{u}}^c + \mathbf{R}_{\mathbf{u}}^{\text{fsi}} + \sum_{i=1}^{n_{\text{tf}}} \mathbf{R}_{\mathbf{u}}^{\text{tf}_i}, \quad (58)$$

where $\mathbf{R}_{\mathbf{u}}^s$ and $\mathbf{K}_{\mathbf{uu}}^s$ are the residual vector and tangent matrix of the solid mechanics problem in absence of contact constraints and fluid flow, computed in a standard way as:

$$\mathbf{R}_{\mathbf{u}}^s = \frac{\partial \Pi^s(\mathbf{u})}{\partial \mathbf{u}}, \quad \mathbf{K}_{\mathbf{uu}}^s = \frac{\partial^2 \Pi^s(\mathbf{u})}{\partial \mathbf{u}^2}. \quad (59)$$

Note that contributions of all trapped fluid zones may be omitted in Eqs. (57)-(58), which gives the possibility to perform simulation of the two-way coupling neglecting the presence of trapped fluid and considering only the effect of fluid pressure in the flow on the deformation of the solid.

It is also important to note that in case of two-way coupling the global matrix defined in (58) is not symmetric, since non-diagonal block terms $\mathbf{K}_{\mathbf{u}p}^f$ and $\mathbf{K}_{p\mathbf{u}}^{\text{fsi}}$ are obtained upon discretization of different equations, see (45) and (49), respectively, and therefore are not equal in the general case. However, if the one-way coupling is considered, these terms vanish, rendering the global tangent matrix symmetric.

The iteration of the Newton-Raphson are performed until the norm of the global residual vector falls below a prescribed tolerance. However, for the coupled problem under study in order to ensure the balance between different fields, we consider separately the norms of the subsets of the residual vector corresponding to different types of DOFs: $\mathbf{R}_{\mathbf{u}}^*$, \mathbf{R}_{λ}^c , \mathbf{R}_p^f , see (57). Therefore, the iterations are performed until all of the following conditions are simultaneously fulfilled:

$$\frac{\|\mathbf{R}_{\mathbf{u}}^*\|_2}{\|\mathbf{R}_{\mathbf{u}}^{\text{ext}}\|_2} < \epsilon_{\mathbf{u}}, \quad \|\mathbf{R}_{\lambda}^c\|_{\infty} < \epsilon_{\lambda}, \quad \|\mathbf{R}_p^f\|_{\infty} < \epsilon_p, \quad (60)$$

where $\epsilon_u, \epsilon_\lambda, \epsilon_p$ are the error tolerance thresholds, chosen separately for each type of the DOF. Note that for the displacements residual \mathbf{R}_u^* we consider the *relative* error, \mathbf{R}^{ext} being the nodal vector related to the external loads, see, for example (Wriggers, 2008), while for the other two residuals we use the *absolute* error criterion. The following notations are used for two different definitions of a norm of a vector \mathbf{R} :

$$\|\mathbf{R}\|_2 = \sqrt{\sum_{i=1}^N R_i^2}, \quad \|\mathbf{R}\|_\infty = \max_{i=1 \dots N} |R_i|, \quad (61)$$

where N is the length of this vector.

4.5.2 Resolution algorithm

Finally, the identification of the local status of the interface remains necessary. During the initialisation of the problem we construct a graph of the interface, vertices of which represent faces of the surface Γ . We consider the so-called “4-connected” (von Neumann) neighbourhood, according to which two faces are connected in this graph if they share an edge, see Fig. 6.

At every iteration of the Newton-Raphson method we perform following steps, summarized in Algorithm 1, which can be easily adjusted to one-way and two-way coupling approaches. We start by identifying active contact elements using the criterion presented in Subsection 4.1, see also Fig. 6(a). Next, in order to locate the fluid-flow domain, we perform the connected-component labelling of non-contact faces using the depth-first search (DFS) (Shapiro, 1996), see Fig. 6(b) and Algorithm 2. Note that this recursive procedure is started from faces which feature fixed pressure due to Dirichlet boundary conditions at least in one node (the set of such nodes can be further divided into inlet and outlet subsets). Once the domain for the flowing fluid is determined, we continue the connected-component labelling of remaining non-contact faces to identify separately each trapped fluid zone, the corresponding procedure is summarized in Algorithm 3, see also Fig. 6(c).

Since the behaviour of each trapped fluid pool depends on the volume of this pool at the moment of its formation, and also on the corresponding average pressure of the fluid inside, a modification of the standard connected-component labelling algorithm is necessary to track creation and evolution of trapped fluid zones. In particular, for each observed trapped fluid pool two cases are possible: some (or all) faces of this zone could have belonged to a trapped fluid zone identified at the end of the previous (converged) loading step, or the considered zone could correspond to a newly trapped fluid pool formed at the current loading step. In the former case, the trapped fluid zone inherits the data (the initial volume and the fluid pressure) from the zone identified at the previous load step. In the latter case, the current volume of a newly created pool is stored and the initial pressure is computed as the mean of the fluid flow pressure values calculated at the end of the previous load step. Note that our study presented below in Subsection 5.1 shows that the fluid flow pressure in a zone which would become trapped at the next load step is very close to being uniform.

It is important to note, that in a simulation with an increasing external load, the splitting of a trapped fluid pool into multiple zones is possible, which will not be recognised by the presented algorithm, i.e. these multiple pools will still be treated as one volume of trapped fluid. However, the effect of this difference on the transmissivity of rough contact interfaces studied in Subsection 5.2, based on the observed results, is not expected to be significant. The opposite process, i.e. the merging of multiple trapped fluid zones into one is also not covered by the presented algorithm. However, this process would require elimination of the contact area between separate pools, while the study of the trapped fluid problem presented in Shvarts and Yastrebov (2018b) shows that a considerable reduction of the contact area corresponds to a significantly higher external load than the one needed for the complete sealing of the interface. Nevertheless, all aforementioned special cases can be included into the presented framework without considerable difficulties. On the other hand, the opening of a trapped zone as described in (Shvarts and Yastrebov, 2018b) coupled to a fluid flow in the interface would necessarily result in a transient process and cannot be accurately taken into account in a quasi-static framework presented here.

Finally, at each iteration we compute the number of local status changes with respect to the previous iteration (or previous converged load step in case of the first iteration). At the i -th iteration this value is calculated as:

$$S^i = \sum_{j=1}^m \begin{cases} 1, & s_j^i \neq s_j^{i-1} \\ 0, & s_j^i = s_j^{i-1} \end{cases}, \quad (62)$$

where m is the total number of faces of the surface Γ , s_j^i is the label of the j -th face of the surface Γ , corresponding to the i -th iteration, and, accordingly, s_j^{i-1} is the label of the same face at the previous

Algorithm 1 Resolution procedure for the coupled problem

Require: $v^i, i = 0$
 1: **procedure** NEWTONRAPHSONLOOP()
 2: **repeat**
 3: **for all** faces of Γ **do**
 4: **if** corresponding contact element is active **then**
 5: face's label \leftarrow CONTACT
 6: **else**
 7: face's label \leftarrow NONE
 8: **end if**
 9: **end for**
 10: **for all** faces with nodes from inlet or outlet **do** //Dirichlet B.C.
 11: DEPTHFIRSTSEARCH(face, FLOW)
 12: **end for**
 13: **for all** faces of Γ **do**
 14: Construct \mathbf{R}^c and \mathbf{K}^c for corresponding contact element
 15: //ALM permits to have contact elements in non-active zone
 16: **if** face's label = FLOW **then**
 17: Construct \mathbf{R}^f and \mathbf{K}^f for corresponding fluid-flow element
 18: **if** two-way coupling **then**
 19: Construct \mathbf{R}^{fsi} and \mathbf{K}^{fsi} for corresponding FSI element
 20: **end if**
 21: **end if**
 22: **if** two-way coupling **then**
 23: IDENTIFYTRAPPEDZONES()
 24: **for all** trapped fluid elements **do**
 25: Construct \mathbf{R}^{tf} and \mathbf{K}^{tf} for trapped-fluid element
 26: **end for**
 27: **end if**
 28: Solve system (57) for Δv^i
 29: $v^{i+1} \leftarrow v^i + \Delta v^i$
 30: $i \leftarrow i + 1$
 31: **until** (60) is validated
 32: **end procedure**

Algorithm 2 Depth-first search (DFS)

1: **procedure** DEPTHFIRSTSEARCH(face, LABEL)
 2: **if** face's label = NONE **then**
 3: face's label \leftarrow LABEL
 4: **for all** neighbours of face **do**
 5: DEPTHFIRSTSEARCH(neighbour, LABEL)
 6: **end for**
 7: **end if**
 8: **end procedure**

Algorithm 3 Trapped fluid zones identification procedure

```

1: procedure IDENTIFYTRAPPEDZONES()
2:   for all trapped fluid elements do //the same list is used for all load steps
3:     if element did not exist at the previous converged load step then
4:       delete trapped fluid element
5:     else
6:       empty element's list of faces
7:     end if
8:   end for
9:   for all faces do
10:    if face's label = NONE then
11:      if face's label at the previous converged load step = TRAP# then
12:        id ← corresponding trapped fluid element's id
13:        DEPTHFIRSTSEARCH(face, TRAP+id) //TRAP1, TRAP2, ...
14:      else
15:        Create new trapped fluid element
16:        id ← new number of trapped fluid elements
17:        DEPTHFIRSTSEARCH(face, TRAP+id) //TRAP1, TRAP2, ...
18:      end if
19:    end if
20:  end for
21:  for all faces do
22:    if face's label = TRAP# then //“#” meaning any number
23:      append face to corresponding element's list of faces
24:    end if
25:  end for
26:  for all trapped fluid elements do
27:    if element did not exist at the previous converged load step then
28:      Compute mean fluid pressure from the previous converged load step
29:      //the initial pressure is the average fluid pressure over all faces of this element
30:    end if
31:  end for
end procedure
    
```

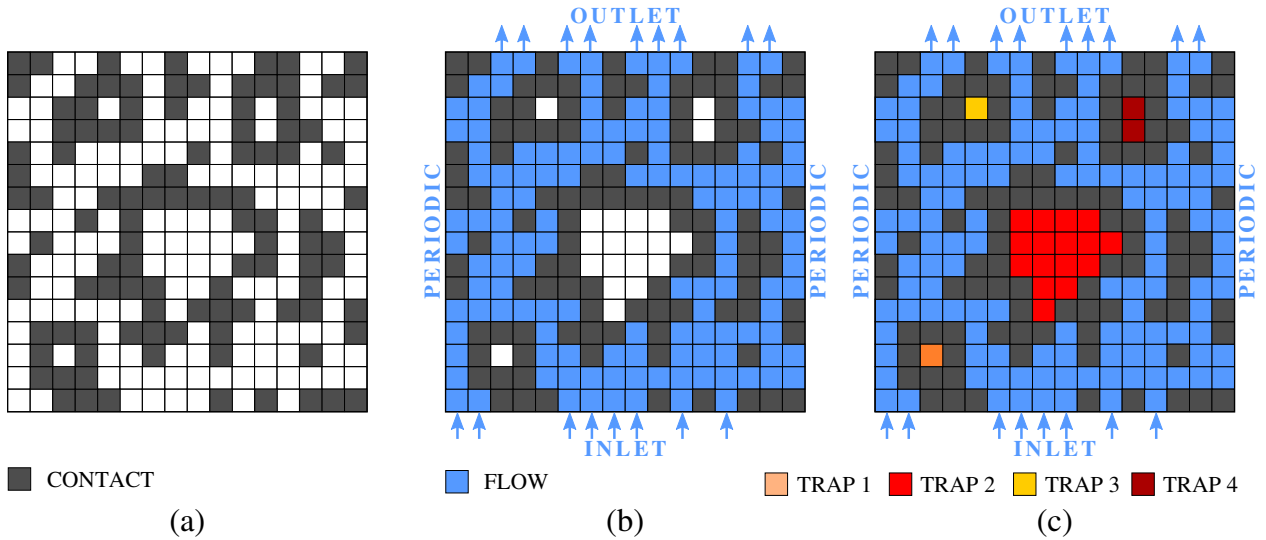


Figure 6: Identification of active contact (a), fluid-flow (b) and trapped fluid zones (c) by performing the connected-component labelling of the interface graph based on the 4-connected neighbourhood: two faces are connected if they share an edge.

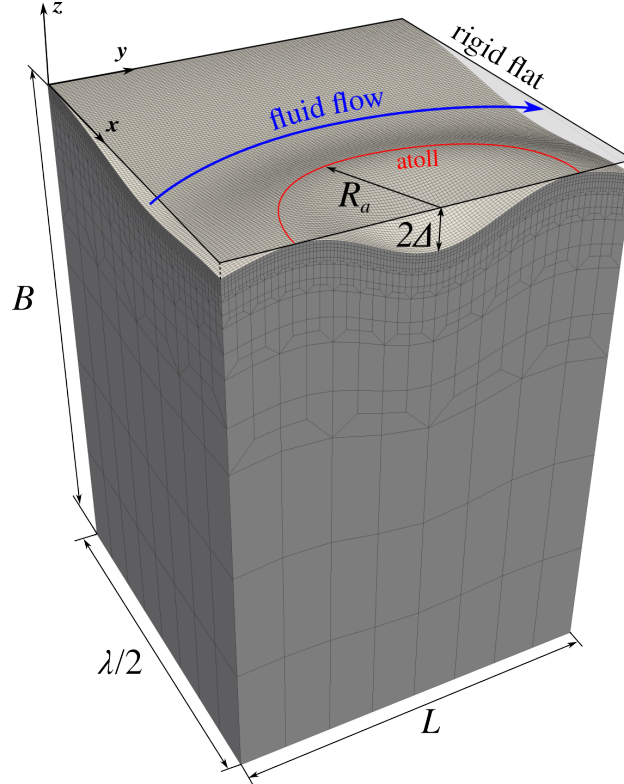


Figure 7: Finite-element mesh with 128×128 faces in the contact interface which was used to solve the problem of the fluid flow across a channel with an “atoll” island. Note that the amplitude of the surface profile is exaggerated to highlight its features, while in the actual simulation the following geometrical parameters were used: $\Delta = 0.02$ mm, $\lambda = 2$ mm, $L = 1$ mm, $B = 1.4$ mm, $R_a = 0.33$ mm, $\alpha = 9$ mm⁻².

iteration (or previous converged load step, if $i = 1$). The label, according to the Algorithm 1, is from the list {CONTACT, FLOW, TRAP#}. At the post-processing stage this number of local status changes permits to study the convergence of the Newton-Raphson method and verify the proposed resolution procedure.

5 Examples and discussions

In this section we present examples which show the capabilities of the proposed framework. In particular, we demonstrate the robustness of the resolution method showing the DOF-wise and status-wise convergence of the Newton-Raphson method and compare two different methods of the contact area computation. Moreover, we show the predictive capabilities of the presented framework regarding the difference between the solutions obtained under one-way and two-way coupling approaches.

5.1 Fluid flow across a wavy channel with an “atoll” island and trapped “lagoon”

We start with presenting an example of a fluid flow in the contact interface which includes also the effect of fluid entrapment. We consider the fluid flow across an extruded wavy channel with an added ring-shaped elevation of the surface at the centre of the channel. Once the solid is gradually brought in contact with a rigid flat, this elevation forms a contact patch in a shape of an “atoll”, which encircles a “lagoon” where the fluid gets trapped, see Fig. 7. The surface of the solid is given by the formula:

$$z(x, y) = \Delta \left(A(x, y) \cos \frac{2\pi x}{\lambda} - 1 \right), \quad (63)$$

$$A(x, y) = 1 - 2\alpha \left[(x - \lambda/2)^2 + (y - L/2)^2 \right] e^{1-\alpha \left[(x - \lambda/2)^2 + (y - L/2)^2 \right]},$$

where Δ and λ are the amplitude and the wavelength of the channel profile, L is the length of the channel, and coefficient α controls the radius of the “atoll” $R_a = 1/\sqrt{\alpha}$. Note that the center of the “lagoon” is at

$(\lambda/2, L/2)$, and the atoll's elevation is equal to the the elevation of the crest on the periphery of the simulated geometry. Therefore, the contact zone will appear simultaneously at the crest of the wavy profile and at the atoll's ridge line.

On vertical faces of the solid we apply zero normal displacement: $\mathbf{u}_y|_{y=0} = \mathbf{u}_y|_{y=L} = 0$ and $\mathbf{u}_x|_{x=0} = \mathbf{u}_x|_{x=\lambda/2} = 0$. The bottom face of the solid is displaced vertically towards the rigid flat within 100 load steps until the fluid channel is completely sealed. We consider throughout the whole loading process a constant fluid pressures prescribed at the inlet: $p|_{y=0} = p_{\text{in}}$ and the outlet $p|_{y=L} = p_{\text{out}}$, accompanied by conditions of zero flux at the remaining part of the boundary of the fluid domain Γ^f : $q_0|_{x=0} = q_0|_{x=\lambda/2} = 0$. Note that due to these boundary conditions $x = 0$ and $x = \lambda/2$ become lines of symmetry of the problem under study.

The geometrical parameters are given in the caption of Fig. 7. For the solid we consider material parameters typical for a soft matter: Young's modulus $E = 1$ GPa and Poisson ratio $\nu = 0.4$ (effective elastic modulus is $E^* = E/(1 - \nu^2) \approx 1.19$ GPa), while fluid parameters are of a typical mineral oil with initial bulk modulus $K_0 = 2$ GPa and $K_1 = 9.25$, see (Kuznetsov, 1985). The inlet fluid pressure is set to $p_{\text{in}} = 10$ MPa and the outlet $p_{\text{out}} = 0$.

The results of the simulation are presented in Fig. 8, note that only three of 100 load steps are shown. At the beginning of the loading, see Fig. 8(a), the atoll's contact zone grows from two opposite (inlet and outlet) sides, therefore the fluid is not yet trapped and is flowing inside the "lagoon". At the same time a contact zone on the crest at $x = 0$ also starts to grow from the outlet side. Note that all contact zones are not symmetric with respect to a line $y = L/2$ (which is the case for the considered geometry if one-way coupling is studied), since the fluid pressure applied to the surface of the solid is maximal at the inlet and is monotonically decreasing towards the outlet. The fluid pressure inside the lagoon before its closure is almost uniform and is higher than the mean value between the inlet and outlet fluid pressures $(p_{\text{in}} + p_{\text{out}})/2$. This is also an effect of considering the two-way coupling, since the fluid pressure decrease from the inlet to the outlet is not linear (which is the case under one-way coupling), but is rather concave, as was shown in (Shvarts and Yastrebov, 2018a). At the second stage, see Fig. 8(b), corresponding to a higher external load, two atoll's zones of contact merge and form a non-simply connected patch, which encircles an out-of-contact lagoon with the trapped fluid inside. Under increasing external pressure, see Fig. 8(c), the contact area continues to grow, reducing the area corresponding to the fluid flow. At the same time, the area of the trapped fluid zone is decreasing much slower due to a higher pressure in the lagoon, which can be observed by comparing the value of stress component σ_{zz} at Γ^{fsi} (bottom of the channel) and at Γ^{tf} (bottom of the lagoon).

5.1.1 Comparison of the interface transmissivity between one- and two-way coupling approaches

In Fig. 9 we present the comparison of the transmissivity of the interface in case of one- and two-way coupling approaches, the latter is presented with and without taking into account the trapped fluid. We compute the effective transmissivity as:

$$K_{\text{eff}} = -\frac{12\mu QL}{\Delta^3(p_{\text{out}} - p_{\text{in}})}, \quad (64)$$

where Q is the mean flux over the area $\lambda/2 \times L$, i.e.

$$Q = \frac{2}{\lambda L} \int_0^{\lambda/2} \int_0^L q_y dx dy, \quad (65)$$

and $q_y = -g^3/(12\mu) \partial p/\partial x$ is the fluid flux in the y -direction.

Under the one-way coupling, which neglects the effect of the fluid pressure on the surface of the solid, the transmissivity of the interface is underestimated. Consequently, the critical pressure needed to seal the channel is higher if the two-way coupling is considered, which is an agreement with (Shvarts and Yastrebov, 2018a), where we found the critical sealing pressure to be an affine function of the inlet pressure for the case of a wavy channel without trapped fluid zone. Moreover, once a trapped fluid pool is formed, it provides additional load-bearing capacity, while its pressure is increasing with the increasing external load. Therefore, the critical sealing pressure is further elevated if the effect of the trapped fluid is taken into account, see Fig. 9.

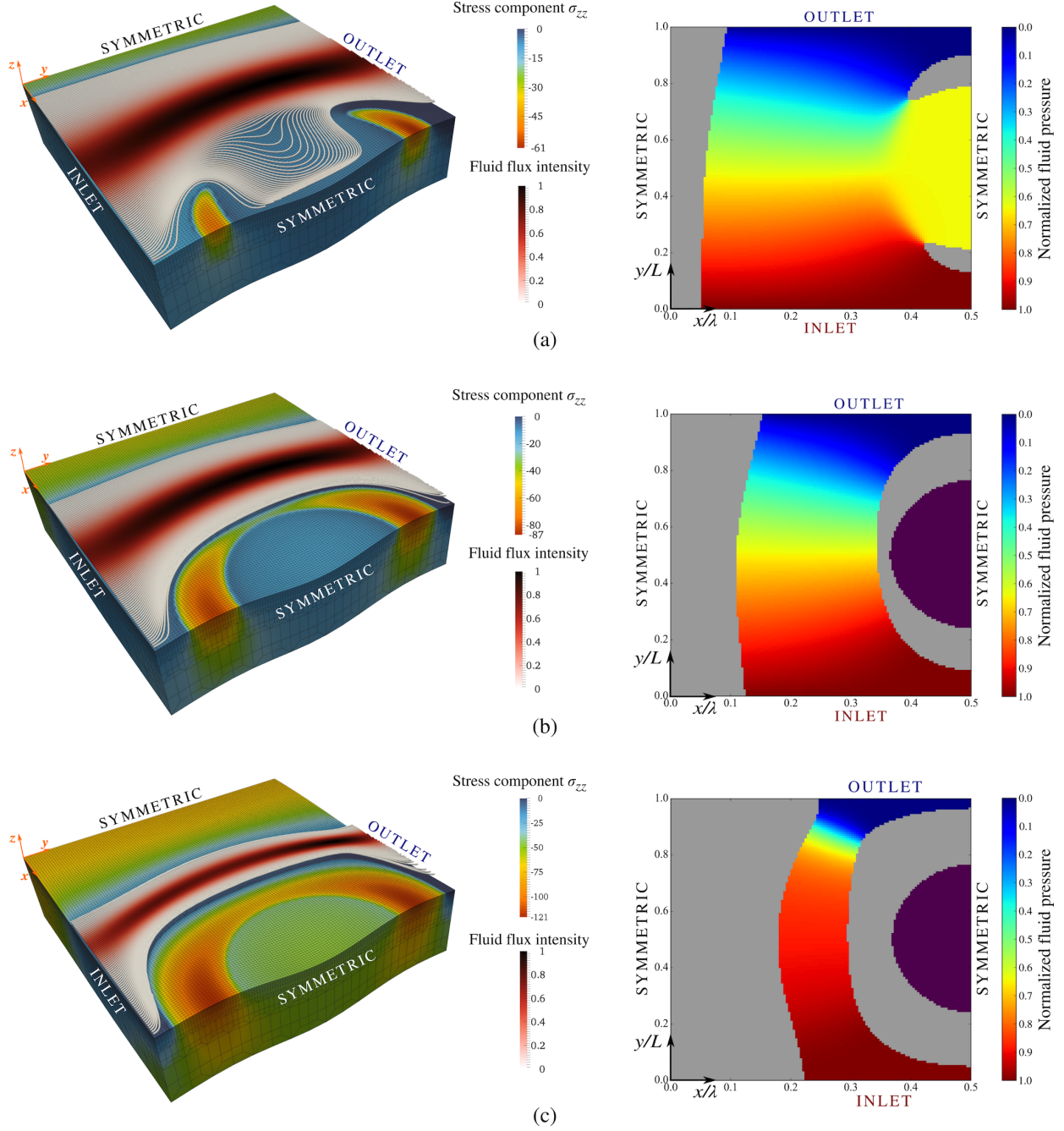


Figure 8: Fluid flow across a wavy channel with an “atoll” island. Three different load steps are presented: (a) beginning of loading, contact occurs only at the crest of channel profile and at two opposite sides of the atoll, therefore fluid is not trapped yet ($p_{\text{ext}}/E^* \cong 0.007$); (b) two atoll’s contact zones merge and fluid is trapped ($p_{\text{ext}}/E^* \cong 0.015$); (c) under increasing load trapped fluid is further pressurized ($p_{\text{ext}}/E^* \cong 0.037$). For each loading step in the left column the bulk view of the solid is shown, with colour representing the σ_{zz} component of the stress tensor, moreover, fluid flow lines with the colour representing the normalized fluid flux intensity q/q_{max} are added. In the right column the interface view is given, with colour representing the normalized fluid pressure in the flow p/p_{in} , the contact patches are shown in grey colour and the trapped fluid zone is purple. Note that the trapped fluid pressure corresponding to loading step (b) is $p^{\text{tf}}/p_{\text{in}} \cong 1.2$, step (c): $p^{\text{tf}}/p_{\text{in}} \cong 4.5$.

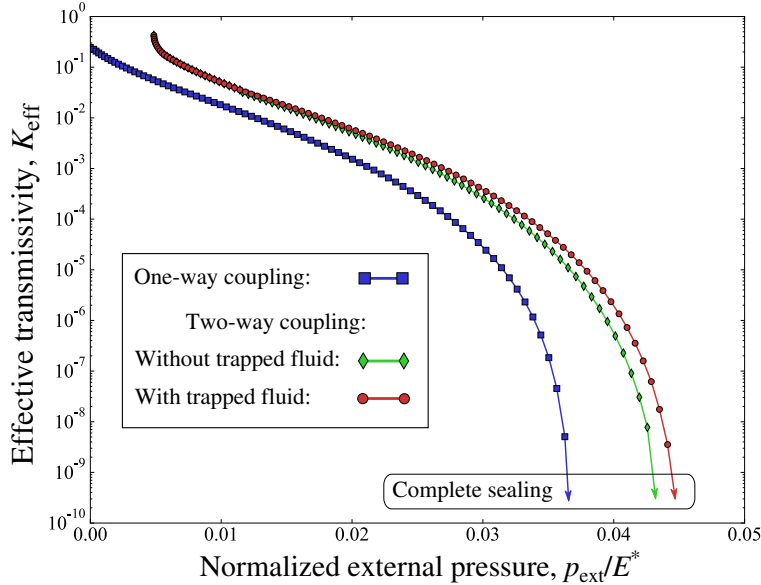


Figure 9: The evolution of the effective interface transmissivity K_{eff} under increasing external load with comparison between 3 simulations: one-way coupling approximation, two-way coupling neglecting effect of the trapped fluid and two-way coupling with the trapped fluid.

5.1.2 Convergence of the Newton-Raphson method

We demonstrate in Fig. 10 the DOF-wise and the status-wise convergence of the Newton-Raphson method corresponding to one particular load step, during which two atoll's contact patches merge and encircle the trapped fluid zone. Note that this step is the most challenging of the whole sequence, since the highest number of local status changes is observed during this step. We present for comparison results obtained in 2 simulations with different values of the fluid inlet pressure: $p_{\text{in}} = 2$ MPa, see Fig. 10(a), and $p_{\text{in}} = 10$ MPa, see Fig. 10(b), while for both cases $p_{\text{out}} = 0$. We also used in both simulations the same tolerance thresholds for different types of DOF: $\epsilon_{\mathbf{u}} = 10^{-6}$, $\epsilon_{\lambda} = \epsilon_p = 10^{-12}$.

According to presented results, while the local status of faces keeps changing between iterations, see (62), the DOF-wise convergence is not quadratic. Note that a high peak of the number of status changes, corresponding to the 2nd iteration in both cases, is caused by the first detection of the trapped fluid zone. However, the number of status changes monotonically decreases after the 2nd iteration. Eventually, the quadratic DOF-wise convergence of the Newton-Raphson method is achieved once the number of status changes reaches zero value, i.e. the partition of the interface remains constant between two iterations. In case of a lower fluid pressure, see Fig. 10(a), the error drops below the specified tolerance after 6 iterations. However, in case of higher fluid pressure, see Fig. 10(b), more iterations are needed to find the correct status for each face. Note also that the quadratic DOF-wise convergence is observed only for displacement DOFs and the Lagrange multipliers, while the norm of the fluid-flow residual $\|\mathbf{R}_p^f\|$ at that iteration is already below the convergence threshold ϵ_p and even close to the double machine precision $\approx 10^{-16}$.

We would like to remark that the parameter ϵ of the augmented Lagrangian method, see (29), was chosen to be $\epsilon = 10^8$ in presented examples. Interestingly, our study showed an unusual dependence of the results on this parameter, which was, however, rather weak. A small oscillation of the surface traction field appeared in the solution at the border between the contact and the fluid flow and/or trapped fluid zones: see surface tractions in the trapped fluid zone in Fig. 8(c), it can be also observed in Fig. 6-8 in Shvarts and Yastrebov (2018a). The reason of this oscillation is probably due to the utilization of the integral (weighted) gap in the contact constraints (26), while for the thin fluid flow the actual nodal gap is used, see (42). Our studies showed that this oscillation is dumped if the value of the augmentation parameter is increased. Unfortunately, ϵ cannot be arbitrary high, since it may lead to bad conditioning of the global tangent matrix. However, the discussed artefact does not affect the solution in the whole domain, and therefore does not undermine the consistency of the proposed method. Nevertheless, it presents an interesting topic of a future investigation.

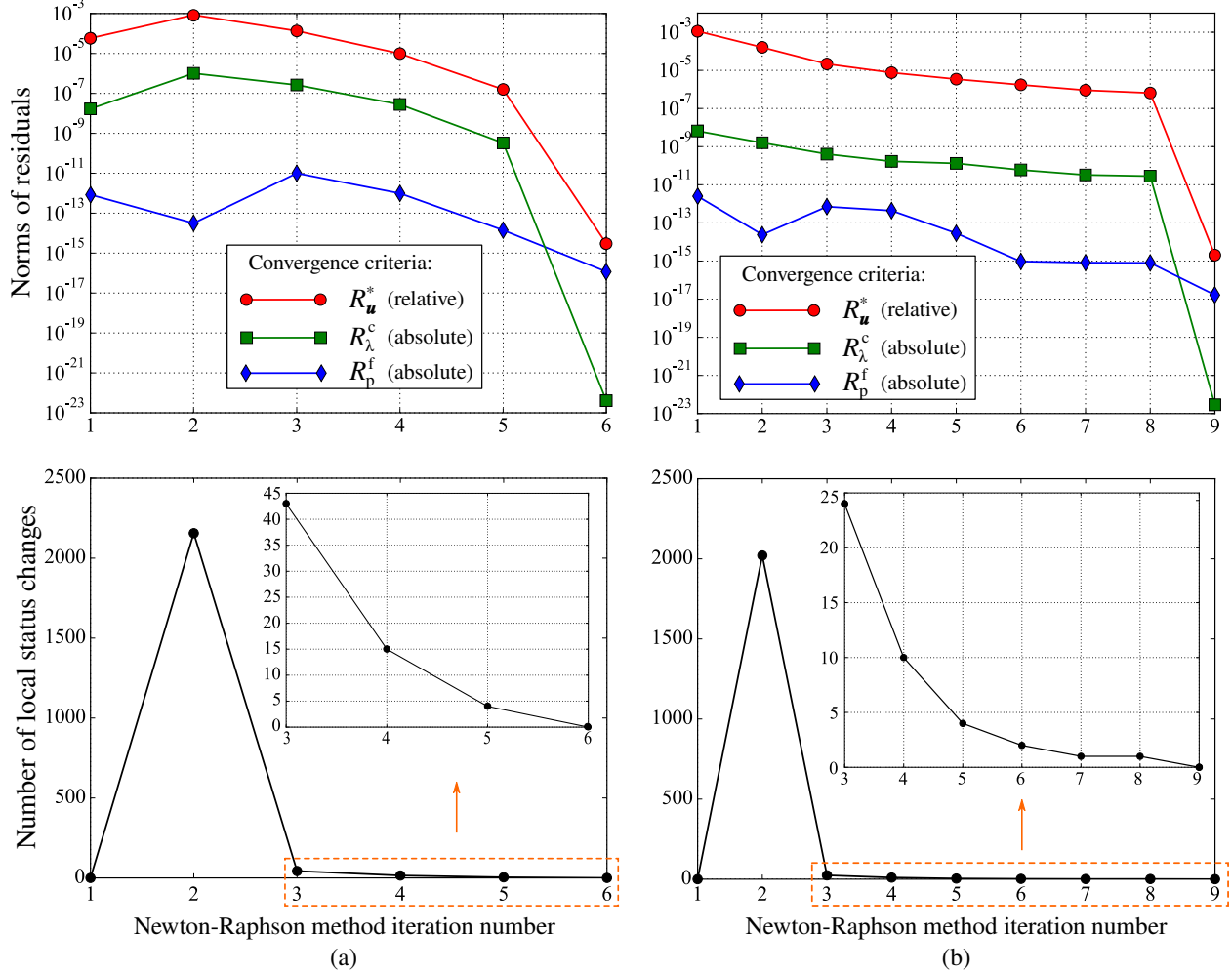


Figure 10: DOF-wise (top) and status-wise (bottom) convergence of the Newton-Raphson method corresponding to a load step during which the trapped fluid zone is formed. Results presented for 2 simulations with different values of the fluid inlet pressure: (a) $p_{\text{in}} = 2$ MPa and (b) $p_{\text{in}} = 10$ MPa. DOF-wise convergence is shown in terms of the relative criterion for the residual corresponding to the displacement DOFs and the absolute criterion for the other two residuals, see (60). The status-wise convergence is shown for the number of status changes defined in (62). Note that the evolution of the number of status changes from the 3rd iteration until the last one is shown in insets for each considered case.

5.2 Fluid flow through representative rough contact interface

The second example is a problem of contact between a deformable solid with a representative *rough* surface and a rigid flat in presence of the thin fluid flow in the free volume between the two surfaces, see Fig. 11 for the sketch of the problem set-up. A physically relevant simulation of a rough surface requires a very fine discretization, which becomes a bottleneck in FEM studies. Therefore, a commonly used approach is to model a part of the surface, which is small enough to make the computation possible, and at the same time big enough to act as a representative surface element, see (Yastrebov et al., 2011; Durand, 2012) for details.

It should be also noted that the spectrum of the roughness has to be rich enough to be physically representative at least to a certain extend, i.e. the frequency cut-offs in the model spectrum need to be chosen with some physical motivation and kept at values for which the continuum mechanics remain a valid approximation, see, for example (Luan and Robbins, 2005). Using the approach discussed in (Yastrebov et al., 2015), we generated a periodic surface with following parameters: smallest wavenumber $k_l = 8\pi/L$ (which corresponds to the longest wavelength $\lambda_l = L/4$), highest wavenumber $k_s = 64\pi/L$ (corresponding to the shortest wavelength $\lambda_s = L/32$), number of points on each side of the surface $N = 256$, Hurst exponent $H = 0.8$.

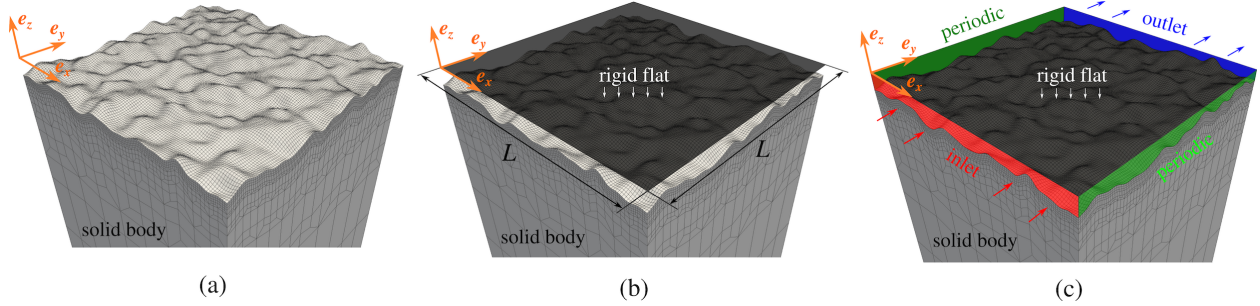


Figure 11: Sketch of the second problem under study: contact between a deformable solid with a periodic representative rough surface (a), brought in contact with a rigid flat (b), in presence of the thin fluid flow in the free volume between the two surfaces (c). Note that the amplitude of the surface roughness is exaggerated, while in the actual simulation we used a surface with root mean squared of heights $S_q = 1 \mu\text{m}$ and rms of the height gradient $S_{dq} \cong 0.055$. The lateral size of the studied square surface is $L = 1 \text{ mm}$, while the vertical size of the FEM mesh $B = 1.4 \text{ mm}$ is the same as in the first example.

Similarly to the first example, we consider throughout the whole loading process a constant fluid pressures prescribed at the inlet: $p|_{y=0} = p_{\text{in}}$ and the outlet $p|_{y=L} = p_{\text{out}}$. However, following the approach of a representative surface element, here we consider periodic boundary conditions at two other sides of the fluid domain: $p|_{x=0} = p|_{x=L}$. According to that, on vertical faces adjacent to the inlet and the outlet zones we apply the boundary conditions of zero normal displacement $\mathbf{u}_y|_{y=0} = \mathbf{u}_y|_{y=L} = 0$, while on two other faces we prescribe the periodic boundary condition: $\mathbf{u}|_{x=0} = \mathbf{u}|_{x=L}$. The bottom face of the solid is displaced vertically towards the rigid flat within 100 load steps until all channels connecting the inlet and the outlet are closed. We use here the same material properties as in the previous example.

Results of the simulation with the fluid inlet pressure $p_{\text{in}} = 4 \text{ MPa}$ and zero outlet pressure are presented in Fig. 12, note that only 3 load steps out of 100 are shown. At the first considered step (a) trapped fluid zones are not yet observed, however, they appear during further loading. Interestingly, atoll-type zones, which were studied previously in a model geometry, appear naturally in case of a representative rough interface, see Fig. 12(b) and (c), at the last presented step the number of these zones is $n_{\text{tf}} = 54$.

It is also important to note, that the spatial distribution of the fluid pressure on its way from the inlet to the outlet changes drastically with the increasing external load. In Fig. 12(a) the pressure decreases rather gradually over the whole interface, with a more rapid change closer to the outlet, which is an effect of considering the two-way coupling. However, under a higher external load, see Fig. 12(b), we observe a certain ‘‘clusterisation’’ of the fluid pressure field, which becomes divided into zones partially surrounded by contact patches. Within these ‘‘clusters’’ the fluid pressure varies little and the intensity of the fluid flow is low, however, the fluid pressure gradient in narrow channels connecting these ‘‘clusters’’ is high. Under the external pressure close to the complete sealing of the interface, see Fig. 12(c), the major part of the fluid-flow domain is under the inlet pressure, while almost all remaining part is under the outlet pressure, and virtually all pressure drop is happening over a narrow constriction connecting these two zones, which is in agreement with theoretical predictions (Persson and Yang, 2008) and previous numerical simulations (Dapp and Müser, 2016), performed under the one-way coupling approach.

5.2.1 Comparison of the interface transmissivity

Similarly to the first example, we compare the effective transmissivity of the contact interface between the representative surface element and a rigid flat in case of one-way and two-way coupling approaches. Considering the representative surface roughness we compute the effective transmissivity as

$$K_{\text{eff}} = -\frac{12\mu QL}{S_q^3(p_{\text{out}} - p_{\text{in}})}, \quad (66)$$

where Q is the mean flux over the apparent contact area $A_0 = L \times L$:

$$Q = \frac{1}{L^2} \int_0^L \int_0^L q_y \, dx dy. \quad (67)$$

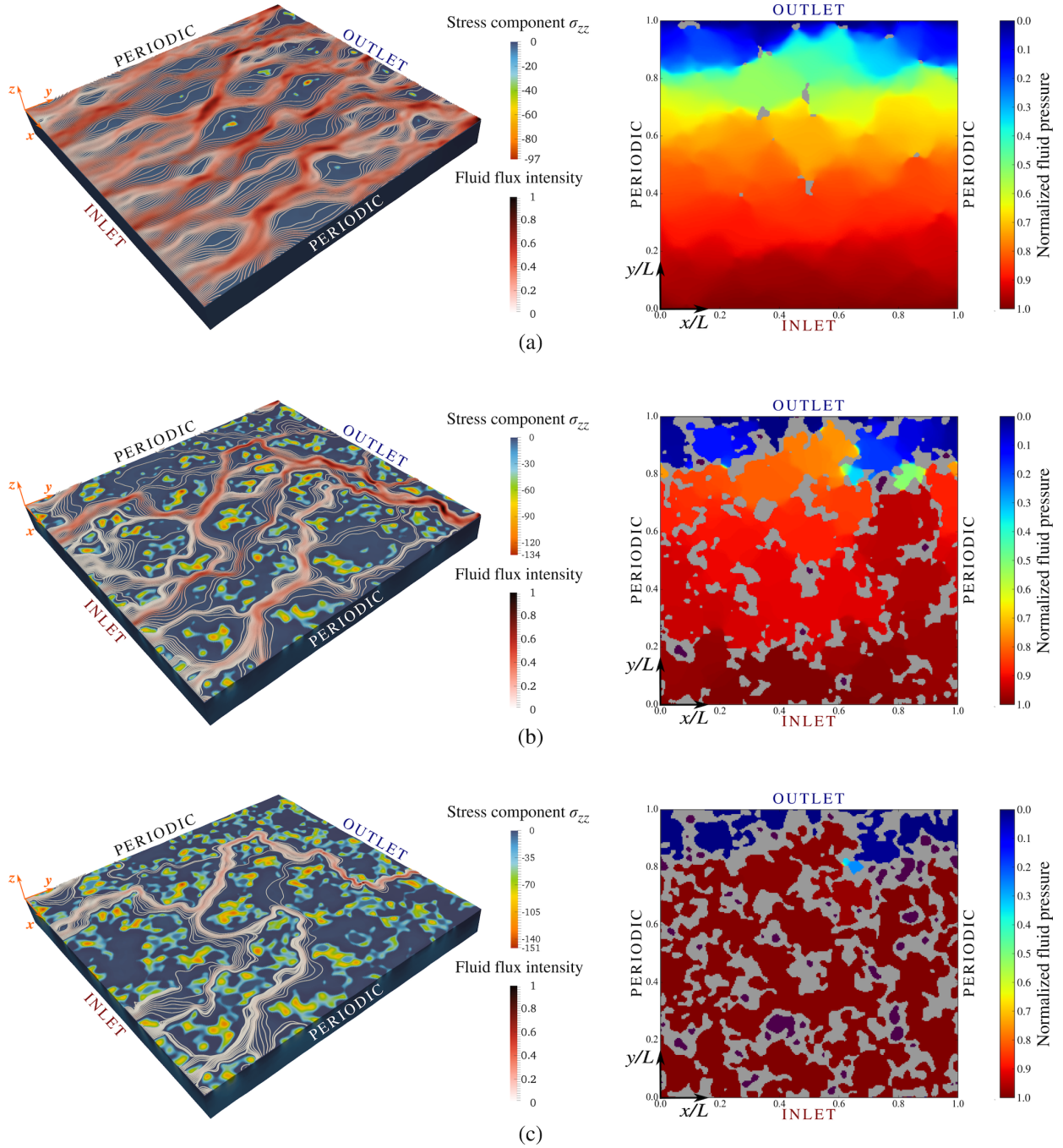


Figure 12: Fluid flow through the contact interface between a deformable solid with representative rough surface and a rigid flat. Three different load steps with increasing external pressure are presented: (a) $p_{\text{ext}}/E^* \cong 0.002$, (b) $p_{\text{ext}}/E^* \cong 0.007$, (c) $p_{\text{ext}}/E^* \cong 0.013$. For each loading step in the left column the bulk view of the solid is shown, with colour on the surface representing the σ_{zz} component of the stress tensor, moreover, fluid flow lines with the colour representing the normalized fluid flux intensity q/q_{max} are added. In the right column the interface view is given, with colour representing the normalized fluid pressure in the flow p/p_{in} , the contact patches are shown in grey colour and all trapped fluid zone are purple (note that the fluid pressure in each trapped zone is different and is increasing with the increasing external loading). At the step (b) 7 trapped fluid zones are present ($n_{\text{tf}} = 7$), the highest trapped fluid pressure is $p^{\text{tf}}/p_{\text{in}} \cong 3.6$, at the step (c) $n_{\text{tf}} = 54$, highest pressure $p^{\text{tf}}/p_{\text{in}} \cong 6.4$.

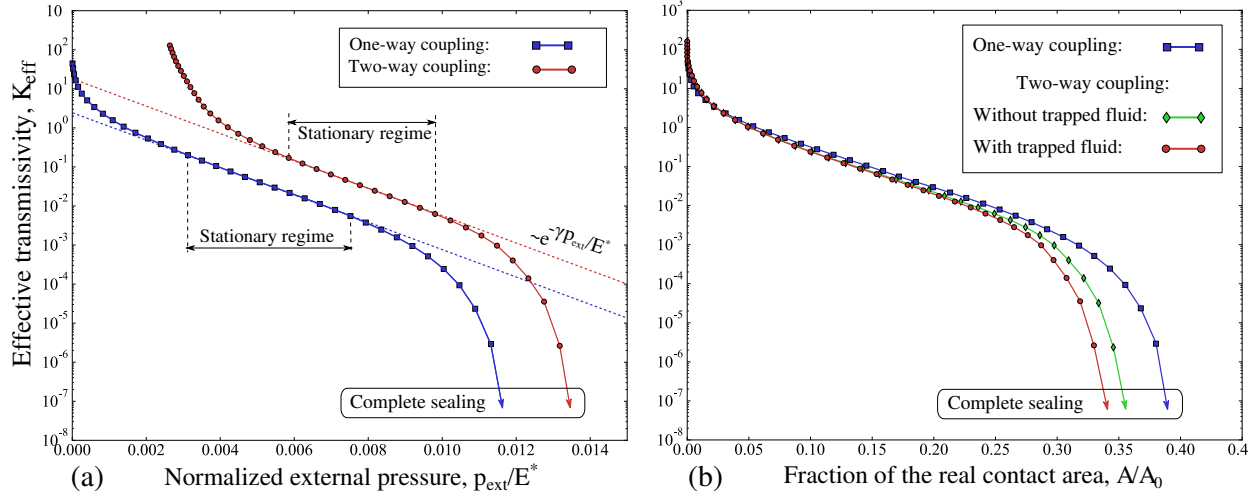


Figure 13: Fluid flow through representative rough contact interface: comparison of the effective transmissivity.

In Fig. 13(a) we present the evolution of the transmissivity under increasing external load. Again we observe a higher transmissivity of the interface (for the same given external pressure) in case of the two-way coupling than under the one-way approach. Consequently, the critical external pressure necessary to completely close the interface for the fluid flow is also higher if the effect of the fluid pressure is taken into account.

Alongside with the critical external pressure, another parameter important for sealing applications is the ratio of the real contact area A to the apparent one $A_0 = L \times L$, computed at the moment when the fluid flow through the interface stops. The corresponding value of A/A_0 is often termed as the *percolation threshold* (Dapp et al., 2012; Dapp and Müser, 2016). These studies, which neglect the effect of the fluid pressure, i.e. are limited to the one-way coupling approach, show that for randomly rough self-affine surfaces $A/A_0 \approx 0.42$ at the percolation.

In Fig. 13(b) we plot the effective transmissivity with respect to the fraction of the real contact area, comparing one-way and two-way coupling (the latter is considered with and without trapped fluid). The percolation threshold is $A/A_0 \approx 0.4$ under the one-way coupling approach, which is in agreement with the aforementioned studies. However, if the two-way coupling is considered (even without trapped fluid), our results show that the same effective transmissivity corresponds to a smaller contact area, than the one observed in the one-way coupling case. Accordingly, the percolation threshold is also lower: $A/A_0 \approx 0.36$. Moreover, if the effect of numerous trapped fluid pools is taken into account, the percolation threshold is further decreased down to $A/A_0 \approx 0.34$. Note that here we used the refined approach to the contact area computation, proposed in Section 4.1.1. The comparison of the two methods of the area computations will be presented below.

5.2.2 Estimation of the range of validity of the one-way coupling approach

We may observe three regimes of the evolution of the effective transmissivity under the increasing external load, see Fig. 13(a). Two of these regimes are transitional: the first one is in the beginning of loading, when the first contact patches form, and the second one is found before the complete sealing (percolation) of the interface. Between these two transitional regimes we observe a stationary phase, where transmissivity is decreasing exponentially with the increasing external load:

$$K_{\text{eff}} \propto e^{-\gamma p_{\text{ext}}/E^*}. \quad (68)$$

In order to quantify the effect of the fluid pressure on the evolution of transmissivity, we performed a set of studies varying the values of inlet and the outlet pressures, and repeating simulations with a number of different realizations of the random surface roughness (keeping statistical parameters the same), see Shvarts (2019) for more details. Finally, we proposed the following formula for fitting the results:

$$\ln K_{\text{eff}} = a_o + \frac{1}{E^*} \left(-\gamma p_{\text{ext}} + \alpha \frac{p_{\text{in}} + p_{\text{out}}}{2} - \beta \frac{p_{\text{out}} - p_{\text{in}}}{L} \right), \quad (69)$$

with the averaged results for fitting parameters:

$$a_o \approx 1.1, \quad \gamma \approx 727.7, \quad \alpha \approx 708.8, \quad \beta \approx 75.7 \text{ [mm]}. \quad (70)$$

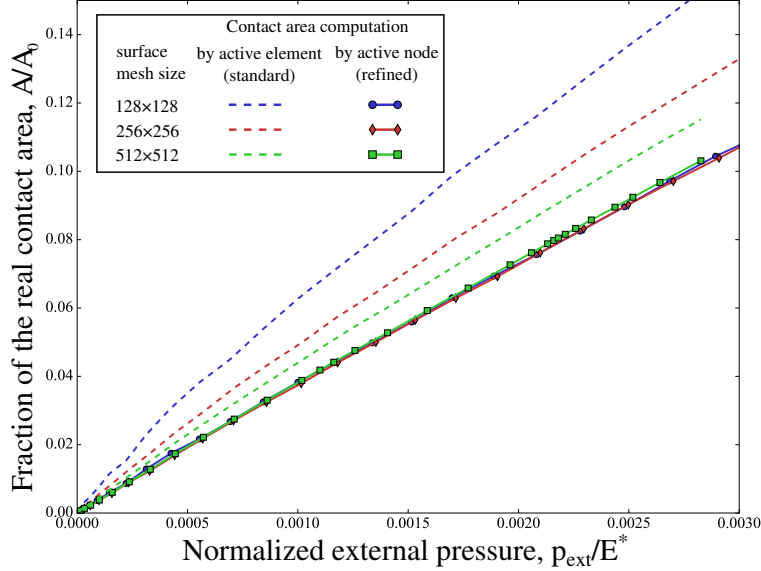


Figure 14: Comparison of two different methods of the real area computation: (39) and (40). Results of simulations using three different meshes are presented (with 128×128 , 256×256 and 512×512 face elements on the surface).

The formula (69) describes the evolution of the effective transmissivity with the increasing external load, depending on the mean fluid pressure and the mean gradient of the fluid pressure, computed over the whole fluid-flow domain. This result can be used for quantitative estimation of the region of validity for the one-way coupling.

Indeed, if the solid is considered linearly elastic, then the sealing external pressure is about $p_{ext} \approx 0.01E^*$ (Yastrebov et al., 2012), meaning that for a soft matter with $E^* \approx 1$ GPa, as in the results of simulations presented above, the sealing pressure is $p_{ext} \approx 10$ MPa. Therefore, the term corresponding to the mean fluid pressure is of the same order of magnitude as the first term in brackets in (69), and the effect of the fluid pressure, observed if the two-way coupling is considered, is significant. However, if the solid is hard, e.g. with $E^* \approx 100$ GPa, then, accordingly, a high external pressure is necessary to seal the interface, such as $p_{ext} \approx 1$ GPa. However, this high pressure is unphysical for fluids used in sealing and lubrication applications. Therefore, the terms in the bracket corresponding to the mean fluid pressure and its gradient are negligible compared to the first term during almost all process of loading, except for the very beginning of it.

5.2.3 Comparison of two methods of the real contact area computation

The real contact area and its morphology are important not only for the study of the percolation in the sealing applications, but represent the key quantity determining the interfacial behaviour in many other physical problems, see (Vakis et al., 2018; Bowden and Tabor, 2001; Pei et al., 2005) for examples. The evolution of the ratio of real contact area to apparent one under increasing external load determines friction, wear, adhesion, as well as electric and heat transfer through contact interfaces. Therefore, it is important to ensure the accurate estimation of the contact area in numerical simulations, see also (Yastrebov et al., 2017). We present in Fig. 14 the comparison of the two methods of the real contact area computation, discussed in Section 4.1.1.

We perform a mesh convergence study, comparing the values of the real contact area obtained in simulations with three different meshes: with 128×128 , 256×256 and 512×512 face elements on the surface Γ , respectively. It is important to note that the spectrum of the surface roughness is preserved exactly the same for all considered meshes. Using the approach discussed in Yastrebov et al. (2015), we generated the surface with following parameters: smallest wavenumber $k_l = 8\pi/L$, highest wavenumber $k_s = 64\pi/L$, Hurst exponent $H = 0.8$. The generated roughness with 513×513 points is mapped on the corresponding mesh. In order to obtain the surface geometry with coarser discretisations (257×257 and 129×129 points), a point-wise sampling was used, which is easy to perform, since the generated finite-element mesh has a regular quadrilateral grid on the surface.

The results show a significant difference between different meshes in case of the contact area computation based on simple summing up of areas of active contact elements, see (39). The convergence seems to take place, but it is very slow. On the contrary, a refined approach to contact area computation (40), that we proposed, leads to a rather mesh-independent calculation of the real contact area.

6 Conclusions

In this paper we propose a monolithic finite-element framework aimed at solving a problem of thin fluid flow in a contact interface between a deformable solid and a rigid flat subject to a normal load. This framework combines a mortar-like augmented-Lagrangian-based contact resolution algorithm, fluid-flow elements for solving the Reynolds equation for incompressible viscous flow between immobile walls and fluid-structure interface elements to apply fluid tractions on the surface of the solid. Additionally, the possibility of fluid entrapment in “pools” delimited by contact patches and its consequent pressurization is considered using a model of compressible fluid with pressure-dependent bulk modulus. This model of the trapped fluid is included into the numerical framework using a “super-element” formulation applied separately for each trapped fluid zone. Furthermore, the proposed framework is suitable for both one- and two-way coupling approaches.

One of the main difficulties of simulating the fluid flow in contact interfaces is associated with the dependency of the extent of fluid-flow domain and the trapped fluid zones on the solution of the contact problem, which can be enhanced by a sophisticated morphology of the contact area resulting from deterministic or random features of the surface geometry. In the developed framework this complexity is handled by an on-flight procedure of partitioning the interface into contact, fluid-flow and trapped fluid zones, performed at each iteration of the Newton-Raphson method using connected-component labelling of the interface graph. The standard algorithm based on the depth-first search was further elaborated to take into account formation and evolution of trapped fluid zones.

To validate the robustness of the proposed monolithic formulation and the efficiency of the resolution algorithm, we considered a model problem with the fluid flow through an extruded wavy a channel with an “atoll”-shaped elevation of the profile, which forms one trapped fluid zone. In particular, we studied DOF-wise and status-wise convergence during the most challenging step of the whole loading sequence, corresponding to the creation of the trapped fluid zone. According to obtained results, the number of status changes is monotonically decreasing after the 2nd iteration, and, moreover, once the local interface status is frozen (i.e. the number of status changes becomes zero) between two Newton-Raphson iterations, the quadratic convergence is achieved.

Furthermore, simulations of the thin fluid flow through a contact interface between a solid with a representative rough surface and a rigid flat were demonstrated. Obtained results are in an agreement with existing theoretical predictions and previous numerical simulations, performed using the one-way coupling approximation. However, the proposed framework permits to highlight the difference between the one-way and two-way coupling approaches, and quantitatively estimate the range of validity of the former. The associated correction of the existing understanding of transmissivity of contact interfaces is important for the sealing engineering, but is also relevant for any problems that involve fluid present in narrow interfaces between solids, e.g. in biological or geophysical applications.

7 Acknowledgments

The authors are grateful to Andreas Almqvist, Francesc Pérez Ràfols, Djamel Missoum-Benziane and Nikolay Osipov for enriching discussions and assistance in the software development. The financial support of Safran Tech, MINES ParisTech and Transvalor is acknowledged.

A Components of the residual vector and tangent matrix

Here we provide detailed expressions for components of residual vectors and tangent matrices formulated above for the contact element (Section 4.1), the thin fluid flow element (Section 4.2) and the fluid-structure interface element (Section 4.3). For all notations used here please refer to the respective Sections.

A.1 Contact element

$$\mathbf{R}_{\mathbf{u}}^c = [\mathbf{R}_{\mathbf{u}_1}^c, \dots, \mathbf{R}_{\mathbf{u}_n}^c]^\top, \quad \mathbf{R}_{\mathbf{u}_j}^c = \sum_{i=1}^n \begin{cases} \hat{\lambda}_i I_{ij} \frac{\partial g_j}{\partial \mathbf{u}_j}, & \hat{\lambda}_i \leq 0 \\ 0, & \hat{\lambda}_i > 0; \end{cases} \quad (71a)$$

$$\mathbf{R}_{\lambda}^c = [\mathbf{R}_{\lambda_1}^c, \dots, \mathbf{R}_{\lambda_n}^c]^\top, \quad \mathbf{R}_{\lambda_i}^c = \begin{cases} \tilde{g}_i, & \hat{\lambda}_i \leq 0 \\ -\frac{1}{\epsilon} \lambda_i, & \hat{\lambda}_i > 0; \end{cases} \quad (71b)$$

$$\mathbf{K}_{\mathbf{u}_k \mathbf{u}_j}^c = \sum_{i=1}^n \begin{cases} \epsilon I_{ij} \frac{\partial g_j}{\partial \mathbf{u}_j} I_{ik} \frac{\partial g_k}{\partial \mathbf{u}_k}, & \hat{\lambda}_i \leq 0 \\ 0, & \hat{\lambda}_i > 0; \end{cases} \quad (71c)$$

$$\mathbf{K}_{\lambda_i \mathbf{u}_j}^c = \mathbf{K}_{\mathbf{u}_j \lambda_i}^c = \begin{cases} I_{ij} \frac{\partial g_j}{\partial \mathbf{u}_j}, & \hat{\lambda}_i \leq 0 \\ 0, & \hat{\lambda}_i > 0; \end{cases} \quad (71d)$$

$$\mathbf{K}_{\lambda_i \lambda_i}^c = \begin{cases} 0, & \hat{\lambda}_i \leq 0 \\ -\frac{1}{\epsilon}, & \hat{\lambda}_i > 0, \end{cases} \quad \mathbf{K}_{\lambda_i \lambda_j}^c = 0 \text{ if } i \neq j. \quad (71e)$$

A.2 Fluid-flow element

$$\mathbf{R}_p^f = [\mathbf{R}_{p_1}^f, \dots, \mathbf{R}_{p_n}^f]^\top, \quad (72a)$$

$$\mathbf{R}_{p_i}^f = \int_{-1}^1 \int_{-1}^1 \left(\sum_{k=1}^n N_k g_k \right)^3 \left(\mathbf{J}^{-1} \sum_{j=1}^n \nabla N_j p_j \right) (\mathbf{J}^{-1} \nabla N_i) \det(\mathbf{J}) d\xi d\eta, \quad (72b)$$

$$\mathbf{K}_{p_i p_j}^f = \int_{-1}^1 \int_{-1}^1 \left(\sum_{k=1}^n N_k g_k \right)^3 (\mathbf{J}^{-1} \nabla N_i) (\mathbf{J}^{-1} \nabla N_j) \det(\mathbf{J}) d\xi d\eta, \quad (72c)$$

$$\mathbf{K}_{\mathbf{u}_l p_i}^f = \frac{\partial g_l}{\partial \mathbf{u}_l} \int_{-1}^1 \int_{-1}^1 3 \left(\sum_{k=1}^n N_k g_k \right)^2 N_l \left(\mathbf{J}^{-1} \sum_{j=1}^n \nabla N_j p_j \right) (\mathbf{J}^{-1} \nabla N_i) \det(\mathbf{J}) d\xi d\eta. \quad (72d)$$

A.3 Fluid-structure interface element

$$\mathbf{R}_{\mathbf{u}_i}^{\text{fsi}} = \sum_{j=1}^n p_j \int_{-1}^1 \int_{-1}^1 \mathbf{n} N_i N_j J d\xi d\eta + \sum_{k=1}^n \frac{g_k}{2} \int_{-1}^1 \int_{-1}^1 \left(\mathbf{J}^{-1} \sum_{l=1}^n \nabla N_l p_l \right) N_i N_k J d\xi d\eta, \quad (73a)$$

$$\mathbf{K}_{\mathbf{u}_k \mathbf{u}_i}^{\text{fsi}} = \frac{1}{2} \frac{\partial g_k}{\partial \mathbf{u}_k} \int_{-1}^1 \int_{-1}^1 \left(\mathbf{J}^{-1} \sum_{l=1}^n \nabla N_l p_l \right) N_i N_k J d\xi d\eta, \quad (73b)$$

$$\mathbf{K}_{p_l \mathbf{u}_i}^{\text{fsi}} = \sum_{k=1}^n \frac{g_k}{2} \int_{-1}^1 \int_{-1}^1 (\mathbf{J}^{-1} \nabla N_l) N_i N_k J d\xi d\eta. \quad (73c)$$

References

- Abaqus 2018 (2018). Theory guide, Dassault Systèmes, Simulia Corp.
- Ager, C., Schott, B., Vuong, A.-T., Popp, A., and Wall, W. A. (2018). A consistent approach for fluid-structure-contact interaction based on a porous flow model for rough surface contact. *International Journal for Numerical Methods in Engineering*.

- Alart, P. and Curnier, A. (1991). A mixed formulation for frictional contact problems prone to newton like solution methods. *Computer methods in applied mechanics and engineering*, 92(3):353–375.
- Astorino, M., Gerbeau, J.-F., Pantz, O., and Traore, K.-F. (2009). Fluid–structure interaction and multi-body contact: application to aortic valves. *Computer Methods in Applied Mechanics and Engineering*, 198(45-46):3603–3612.
- Azushima, A. and Kudo, H. (1995). Direct Observation of Contact Behaviour to Interpret the Pressure Dependence of the Coefficient of Friction in Sheet Metal Forming. *CIRP Annals - Manufacturing Technology*, 44(1):209–212.
- Baaijens, F. P. (2001). A fictitious domain/mortar element method for fluid–structure interaction. *International Journal for Numerical Methods in Fluids*, 35(7):743–761.
- Barber, J. R. (2013). Incremental stiffness and electrical contact conductance in the contact of rough finite bodies. *Phys Rev E*, 87:013203.
- Bažant, Z. P., Salviato, M., Chau, V. T., Viswanathan, H., and Zubelewicz, A. (2014). Why fracking works. *Journal of Applied Mechanics*, 81(10):101010.
- Bazilevs, Y., Calo, V. M., Zhang, Y., and Hughes, T. J. (2006). Isogeometric fluid–structure interaction analysis with applications to arterial blood flow. *Computational Mechanics*, 38(4-5):310–322.
- Bazilevs, Y., Hsu, M.-C., Kiendl, J., Wüchner, R., and Bletzinger, K.-U. (2011). 3d simulation of wind turbine rotors at full scale. part ii: Fluid–structure interaction modeling with composite blades. *International Journal for Numerical Methods in Fluids*, 65(1-3):236–253.
- Besson, J. and Foerch, R. (1997). Large scale object-oriented finite element code design. *Computer Methods in Applied Mechanics and Engineering*, 142:165–187.
- Bowden, F. P. and Tabor, D. (2001). *The Friction and Lubrication of Solids*. Oxford University Press.
- Brown, S. R., Stockman, H. W., and Reeves, S. J. (1995). Applicability of the reynolds equation for modeling fluid flow between rough surfaces. *Geophysical Research Letters*, 22(18):2537–2540.
- Caligaris, M. and Ateshian, G. A. (2008). Effects of sustained interstitial fluid pressurization under migrating contact area, and boundary lubrication by synovial fluid, on cartilage friction. *Osteoarthritis and Cartilage*, 16(10):1220–1227.
- Cavaliere, F. J. and Cardona, A. (2013). An augmented lagrangian technique combined with a mortar algorithm for modelling mechanical contact problems. *International Journal for Numerical Methods in Engineering*, 93(4):420–442.
- Chan, S., Neu, C., Komvopoulos, K., and Reddi, A. (2011). The role of lubricant entrapment at biological interfaces: Reduction of friction and adhesion in articular cartilage. *Journal of biomechanics*, 44(11):2015–2020.
- Dapp, W. B., Lücke, A., Persson, B. N. J., and Müser, M. H. (2012). Self-affine elastic contacts: Percolation and leakage. *Phys Rev Lett*, 108:244301.
- Dapp, W. B. and Müser, M. H. (2016). Fluid leakage near the percolation threshold. *Scientific reports*, 6:19513.
- De Hart, J., Peters, G., Schreurs, P., and Baaijens, F. (2003). A three-dimensional computational analysis of fluid–structure interaction in the aortic valve. *Journal of biomechanics*, 36(1):103–112.
- Donea, J., Giuliani, S., and Halleux, J.-P. (1982). An arbitrary lagrangian-eulerian finite element method for transient dynamic fluid-structure interactions. *Computer methods in applied mechanics and engineering*, 33(1-3):689–723.
- Dos Santos, N. D., Gerbeau, J.-F., and Bourgat, J.-F. (2008). A partitioned fluid–structure algorithm for elastic thin valves with contact. *Computer Methods in Applied Mechanics and Engineering*, 197(19-20):1750–1761.
- Durand, J. (2012). *Multiscale Modelling of Contact of Rough Surfaces*. PhD thesis, MINES ParisTech, PSL Research University.
- Farhat, C., Geuzaine, P., and Brown, G. (2003). Application of a three-field nonlinear fluid–structure formulation to the prediction of the aeroelastic parameters of an f-16 fighter. *Computers & Fluids*, 32(1):3–29.
- Farhat, C., Lesoinne, M., and Le Tallec, P. (1998). Load and motion transfer algorithms for fluid/structure interaction problems with non-matching discrete interfaces: Momentum and energy conservation, optimal discretization and application to aeroelasticity. *Computer methods in applied mechanics and engineering*, 157(1-2):95–114.

- Fischer, U. H. and Clarke, G. K. (1997). Stick slip sliding behaviour at the base of a glacier. *Annals of Glaciology*, 24:390–396.
- Garagash, D. I. and Germanovich, L. N. (2012). Nucleation and arrest of dynamic slip on a pressurized fault. *Journal of Geophysical Research: Solid Earth*, 117(B10).
- Gerbeau, J.-F. and Vidrascu, M. (2003). A quasi-newton algorithm based on a reduced model for fluid-structure interaction problems in blood flows. *ESAIM: Mathematical Modelling and Numerical Analysis*, 37(4):631–647.
- Gerstenberger, A. and Wall, W. A. (2008). An extended finite element method/lagrange multiplier based approach for fluid–structure interaction. *Computer Methods in Applied Mechanics and Engineering*, 197(19-20):1699–1714.
- Hamrock, B. J., Schmid, S. R., and Jacobson, B. O. (2004). *Fundamentals of fluid film lubrication*. CRC press.
- Heil, M. (1998). Stokes flow in an elastic tube—a large-displacement fluid-structure interaction problem. *International journal for numerical methods in fluids*, 28(2):243–265.
- Heil, M. (2004). An efficient solver for the fully coupled solution of large-displacement fluid–structure interaction problems. *Computer Methods in Applied Mechanics and Engineering*, 193(1-2):1–23.
- Hubbert, M. K. and Willis, D. G. (1972). *Mechanics of hydraulic fracturing*. AAPG Special Volumes.
- Hübner, B., Walhorn, E., and Dinkler, D. (2004). A monolithic approach to fluid–structure interaction using space–time finite elements. *Computer methods in applied mechanics and engineering*, 193(23-26):2087–2104.
- Kadapa, C., Dettmer, W., and Perić, D. (2017). A stabilised immersed boundary method on hierarchical b-spline grids for fluid–rigid body interaction with solid–solid contact. *Computer Methods in Applied Mechanics and Engineering*, 318:242–269.
- Kamensky, D., Hsu, M.-C., Schillinger, D., Evans, J. A., Aggarwal, A., Bazilevs, Y., Sacks, M. S., and Hughes, T. J. (2015). An immersogeometric variational framework for fluid–structure interaction: Application to bioprosthetic heart valves. *Computer methods in applied mechanics and engineering*, 284:1005–1053.
- Kikuchi, N. and Oden, J. T. (1988). *Contact problems in elasticity: a study of variational inequalities and finite element methods*, volume 8. siam.
- Konyukhov, A. and Schweizerhof, K. (2012). *Computational Contact Mechanics: geometrically exact theory for arbitrary shaped bodies*, volume 67. Springer Science & Business Media.
- Krim, J. and Palasantzas, G. (1995). Experimental observations of self-affine scaling and kinetic roughening at sub-micron lengthscales. *Int J Mod Phys B*, 9:599–632.
- Küttler, U. and Wall, W. A. (2008). Fixed-point fluid–structure interaction solvers with dynamic relaxation. *Computational Mechanics*, 43(1):61–72.
- Kuznetsov, Y. (1985). Effect of fluid lubricant on the contact characteristics of rough elastic bodies in compression. *Wear*, 102(3):177–194.
- Lorenz, B. and Persson, B. (2010). Time-dependent fluid squeeze-out between solids with rough surfaces. *The European Physical Journal E*, 32(3):281–290.
- Luan, B. and Robbins, M. O. (2005). The breakdown of continuum models for mechanical contacts. *Nature*, 435:929–932.
- Matthies, H. G. and Steindorf, J. (2003). Partitioned strong coupling algorithms for fluid–structure interaction. *Computers & structures*, 81(8-11):805–812.
- Mayer, U. M., Popp, A., Gerstenberger, A., and Wall, W. A. (2010). 3d fluid–structure-contact interaction based on a combined xfm fsi and dual mortar contact approach. *Computational Mechanics*, 46(1):53–67.
- Michler, C., Hulshoff, S., Van Brummelen, E., and De Borst, R. (2004). A monolithic approach to fluid–structure interaction. *Computers & fluids*, 33(5-6):839–848.
- Mittal, R. and Iaccarino, G. (2005). Immersed boundary methods. *Annu. Rev. Fluid Mech.*, 37:239–261.
- Müller, H. K. and Nau, B. S. (1998). *Fluid Sealing Technology: Principles and Applications*. M. Dekker.
- Nayak, P. R. (1971). Random process model of rough surfaces. *J Lubr Technol (ASME)*, 93:398–407.
- Païdoussis, M. P., Price, S. J., and De Langre, E. (2010). *Fluid-structure interactions: cross-flow-induced instabilities*. Cambridge University Press.

- Patir, N. and Cheng, H. (1978). An average flow model for determining effects of three-dimensional roughness on partial hydrodynamic lubrication. *Trans. ASME, J. Lubr. Technol.*, 100:12–17.
- Pei, L., Hyun, S., Molinari, J. F., and Robbins, M. O. (2005). Finite element modeling of elasto-plastic contact between rough surfaces. *J Mech Phys Solids*, 53:2385–2409.
- Pérez-Ràfols, F., Larsson, R., and Almqvist, A. (2016). Modelling of leakage on metal-to-metal seals. *Tribology International*, 94:421 – 427.
- Pérez-Ràfols, F., Larsson, R., Lundström, S., Wall, P., and Almqvist, A. (2016). A stochastic two-scale model for pressure-driven flow between rough surfaces. *Proceedings of the Royal Society A: Mathematical, Physical and Engineering Sciences*, 472(2190):20160069.
- Persson, B. and Yang, C. (2008). Theory of the leak-rate of seals. *Journal of Physics: Condensed Matter*, 20(31):315011.
- Ponson, L., Bonamy, D., Auradou, H., Mourot, G., Morel, S., Bouchaud, E., Guillot, C., and Hulin, J. P. (2006). Anisotropic self-affine properties of experimental fracture surfaces. *Int J Fracture*, 140(1):27–37.
- Prodanov, N., Gachot, C., Rosenkranz, A., Mücklich, F., and Müser, M. H. (2013). Contact mechanics of laser-textured surfaces. *Tribology Letters*, 50(1):41–48.
- Puso, M. A. (2004). A 3D mortar method for solid mechanics. *International Journal for Numerical Methods in Engineering*, 59(3):315–336.
- Puso, M. A., Laursen, T., and Solberg, J. (2008). A segment-to-segment mortar contact method for quadratic elements and large deformations. *Computer Methods in Applied Mechanics and Engineering*, 197(6-8):555–566.
- Puso, M. A. and Laursen, T. A. (2004). A mortar segment-to-segment contact method for large deformation solid mechanics. *Computer methods in applied mechanics and engineering*, 193(6):601–629.
- Sahlin, F., Larsson, R., Almqvist, A., Lugt, P. M., and Marklund, P. (2010a). A mixed lubrication model incorporating measured surface topography. part 1: Theory of flow factors. *Proceedings of the Institution of Mechanical Engineers, Part J: Journal of Engineering Tribology*, 224(4):335–351.
- Sahlin, F., Larsson, R., Marklund, P., Almqvist, A., and Lugt, P. (2010b). A mixed lubrication model incorporating measured surface topography. part 2: roughness treatment, model validation, and simulation. *Proceedings of the Institution of Mechanical Engineers, Part J: Journal of Engineering Tribology*, 224(4):353–365.
- Scaraggi, M. and Persson, B. (2012). Time-dependent fluid squeeze-out between soft elastic solids with randomly rough surfaces. *Tribology letters*, 47(3):409–416.
- Sergeant, A., Yastrebov, V. A., Mangeney, A., Castelnaud, O., Montagner, J.-P., and Stutzmann, E. (2018). Numerical modeling of iceberg capsizing responsible for glacial earthquakes. *Journal of Geophysical Research: Earth Surface*, 123(11):3013–3033.
- Shapiro, L. G. (1996). Connected component labeling and adjacency graph construction. In *Machine Intelligence and Pattern Recognition*, volume 19, pages 1–30. Elsevier.
- Shvarts, A. (2019). *Coupling mechanical frictional contact with interfacial fluid flow at small and large scales*. PhD thesis, MINES ParisTech, PSL Research University.
- Shvarts, A. G. and Yastrebov, V. A. (2018a). Fluid flow across a wavy channel brought in contact. *Tribology International*, 126:116–126.
- Shvarts, A. G. and Yastrebov, V. A. (2018b). Trapped fluid in contact interface. *Journal of the Mechanics and Physics of Solids*.
- Soltz, M. A., Basalo, I. M., and Ateshian, G. A. (2003). Hydrostatic pressurization and depletion of trapped lubricant pool during creep contact of a rippled indenter against a biphasic articular cartilage layer. *Journal of biomechanical engineering*, 125(5):585–593.
- Stupkiewicz, S. (2009). Finite element treatment of soft elastohydrodynamic lubrication problems in the finite deformation regime. *Computational Mechanics*, 44(5):605–619.
- Stupkiewicz, S. (2018). Finite wear and soft elasto-hydrodynamic lubrication: Beyond the classical frictional contact of soft solids. In Popp, A. and Wriggers, P., editors, *Contact Modeling for Solids and Particles*, volume 585, chapter 3, pages 125–176. Springer.
- Stupkiewicz, S., Lengiewicz, J., Sadowski, P., and Kucharski, S. (2016). Finite deformation effects in soft elastohydrodynamic lubrication problems. *Tribology International*, 93:511–522.

- Stupkiewicz, S. and Marcinişzyn, A. (2009). Elastohydrodynamic lubrication and finite configuration changes in reciprocating elastomeric seals. *Tribology International*, 42(5):615–627.
- Takashi, N. and Hughes, T. J. (1992). An arbitrary lagrangian-eulerian finite element method for interaction of fluid and a rigid body. *Computer methods in applied mechanics and engineering*, 95(1):115–138.
- Thomas, T. R. (1999). *Rough Surfaces*. Imperial College Press, second edition.
- Vakis, A., Yastrebov, V., Scheibert, J., Minfray, C., Nicola, L., Dini, D., Almqvist, A., Paggi, M., Lee, S., Limbert, G., et al. (2018). Modeling and simulation in tribology across scales: An overview. *Tribology International*.
- Verdugo, F. and Wall, W. A. (2016). Unified computational framework for the efficient solution of n-field coupled problems with monolithic schemes. *Computer Methods in Applied Mechanics and Engineering*, 310:335–366.
- Viesca, R. C. and Rice, J. R. (2012). Nucleation of slip-weakening rupture instability in landslides by localized increase of pore pressure. *Journal of Geophysical Research: Solid Earth (1978–2012)*, 117(B3).
- Wackers, J., Koren, B., Raven, H. C., Van der Ploeg, A., Starke, A., Deng, G., Queutey, P., Visonneau, M., Hino, T., and Ohashi, K. (2011). Free-surface viscous flow solution methods for ship hydrodynamics. *Archives of Computational Methods in Engineering*, 18(1):1–41.
- Waseem, A., Guilleminot, J., and Temizer, I. (2017). Stochastic multiscale analysis in hydrodynamic lubrication. *International Journal for Numerical Methods in Engineering*, 112(8):1070–1093.
- Westergaard, H. M. (1939). Bearing pressures and cracks. *J Appl Mech (ASME)*, 6:49.
- Whitehouse, D. J. (2010). *Handbook of surface and nanometrology*. CRC press.
- Wick, T. (2014). Flapping and contact fsi computations with the fluid–solid interface-tracking/interface-capturing technique and mesh adaptivity. *Computational Mechanics*, 53(1):29–43.
- Wriggers, P. (2006). *Computational Contact Mechanics*. Springer, Berlin, Heidelberg.
- Wriggers, P. (2008). *Nonlinear finite element methods*. Springer Science & Business Media.
- Yang, B. and Laursen, T. A. (2009). A mortar-finite element approach to lubricated contact problems. *Computer Methods in Applied Mechanics and Engineering*, 198(47):3656–3669.
- Yastrebov, V. A. (2013). *Numerical methods in contact mechanics*. John Wiley & Sons.
- Yastrebov, V. A., Anciaux, G., and Molinari, J. F. (2012). Contact between representative rough surfaces. *Phys Rev E*, 86(3):035601(R).
- Yastrebov, V. A., Anciaux, G., and Molinari, J.-F. (2015). From infinitesimal to full contact between rough surfaces: evolution of the contact area. *International Journal of Solids and Structures*, 52:83–102.
- Yastrebov, V. A., Anciaux, G., and Molinari, J.-F. (2017). On the accurate computation of the true contact-area in mechanical contact of random rough surfaces. *Tribology International*, 114:161–171.
- Yastrebov, V. A., Durand, J., Proudhon, H., and Cailletaud, G. (2011). Rough surface contact analysis by means of the finite element method and of a new reduced model. *Comptes Rendus Mécanique*, 339(7):473–490.
- Z-set (2019). Non-linear material and structure analysis suite, version 9.0. MINES ParisTech and Onera, the French Aerospace Lab. <http://www.zset-software.com>.
- Zaouter, T., Lasseux, D., and Prat, M. (2018). Gas slip flow in a fracture: local reynolds equation and upscaled macroscopic model. *Journal of Fluid Mechanics*, 837:413–442.
- Zienkiewicz, O. C. and Taylor, R. L. (1977). *The finite element method*. McGraw-Hill London.